

# Thermodynamic and transport properties of RAgGe (R=Tb-Lu) single crystals

E. Morosan,<sup>a,b</sup> S. L. Bud'ko,<sup>a</sup> P. C. Canfield,<sup>a,b</sup>  
M. S. Torikachvili,<sup>c</sup> A. H. Lacerda<sup>d</sup>

<sup>a</sup>Ames Laboratory U.S. D.O.E., Iowa State University, Ames, IA 50011

<sup>b</sup>Department of Physics and Astronomy, Iowa State University, Ames, IA 50011

<sup>c</sup>Department of Physics, San Diego State University, San Diego, CA 92182

<sup>d</sup>National High Magnetic Field Laboratory, Los Alamos Facility, Los Alamos  
National Laboratory, Los Alamos, NM 87545

---

## Abstract

Single crystals of the title compounds were grown out of an AgGe-rich ternary solution. Powder x-ray diffraction data confirmed the hexagonal AlNiZr-type structure ( $P\bar{6}2m$  space group), an ordered variant of the Fe<sub>2</sub>P structure type. Antiferromagnetic ordering can be inferred from magnetization, resistance and specific heat measurements, with values of  $T_N$  between 28.5 K for TbAgGe, and 1.0 K for YbAgGe, which scale roughly with the de Gennes factor. Anisotropic  $M(H)$  measurements indicate one or more metamagnetic transitions when the external field is applied along the  $c$ -axis (for R=Tb) or perpendicular to it (R = Ho, Er, Tm), or even in both orientations as in the case of DyAgGe. Furthermore, the extreme anisotropy of the magnetization in TmAgGe, where magnetic moments lie in the  $ab$ -plane, provides the possibility of studying the angular dependence of metamagnetism in hexagonal compounds with the rare earth in orthorhombic point symmetry.

YbAgGe has distinct properties from the rest of the series: an enhanced electronic specific heat coefficient ( $\gamma \approx (154.2 \pm 2.5) \text{ mJ/mol} \cdot \text{K}^2$ ), and apparently small moment magnetic ordering below 1.0 K. This compound appears to be close to a quantum critical point.

*Key words:*

RAgGe, crystal electric field, local moment magnetism, metamagnetism, heavy fermion

*PACS:* 75.30.Kz, 75.30.Gw,, 75.30.Mb, 75.50.Ee

---

## 1 Introduction

Ternary intermetallic compounds R-T-M, with R=rare earth metals, T=transition metals, M=metals of the  $p$  block, have raised a lot of interest in the past years, given their structural complexity and their greatly varying physical properties. Studies of the anisotropic properties of such materials, with the R in tetragonal point symmetry, revealed anisotropy (in some cases extreme) in members of the RAgSb<sub>2</sub> [1] and RNi<sub>2</sub>Ge<sub>2</sub> [2] series, as well as in the well known quaternary RNi<sub>2</sub>B<sub>2</sub>C compounds, for R=Tb-Er [3,4,5,6]. The strong crystalline electric field (CEF) anisotropy confines the moments either along the  $c$ -axis of the tetragonal unit cell (i.e. in TbNi<sub>2</sub>Ge<sub>2</sub>, ErAgSb<sub>2</sub>, TmAgSb<sub>2</sub>), or to the basal plane  $ab$  (in ErNi<sub>2</sub>Ge<sub>2</sub>, DyAgSb<sub>2</sub> and the aforementioned RNi<sub>2</sub>B<sub>2</sub>C compounds), and metamagnetic transitions occur in the majority of these materials. TbNi<sub>2</sub>Ge<sub>2</sub> was chosen for an extensive study of angular dependent metamagnetism in an axial (Ising-like) compound [2], showing fairly simple angular dependencies of locally saturated magnetizations ( $M_{sat}(\theta)$ ) and critical fields ( $H_c(\theta)$ ). The complexity of the  $M_{sat}(\theta)$  and  $H_c(\theta)$  phase diagrams drastically increases for systems where the magnetic moments are confined to the  $ab$ -plane, as shown by the detailed analysis of  $M(H, \theta)$  data done for HoNi<sub>2</sub>B<sub>2</sub>C [3] and DyAgSb<sub>2</sub> [7]. Furthermore, a theoretical model has been developed by Kalatsky and Pokrovsky [8], to explain the experimentally observed behavior of metamagnetism in HoNi<sub>2</sub>B<sub>2</sub>C. An appropriate variant of this four-position clock model subsequently agreed with the data on DyAgSb<sub>2</sub> [7].

In addition to metamagnetism, hybridization of the  $4f$  moments occurs in some compounds, making these tetragonal series even more interesting: YbNi<sub>2</sub>B<sub>2</sub>C [9], CeNi<sub>2</sub>Ge<sub>2</sub> [2,10], YbNi<sub>2</sub>Ge<sub>2</sub> [2] are reported to have significant hybridization between the  $4f$  and the conduction electrons.

Having achieved a basic understanding of the physical properties of these tetragonal compounds, in which the R<sup>3+</sup> ions are positioned in crystallographically unique tetragonal point symmetry sites, we anticipate that materials with different crystal structure would be of further interest. Crystals with hexagonal unit cells preserve the axial versus basal plane anisotropy while allowing for three interesting R point symmetries: orthorhombic, trigonal or hexagonal. A representative of the first class of materials (i.e. orthorhombic point symmetry) is the RAgGe series, that crystallizes in the AlNiZr structure, an ordered variant of the Fe<sub>2</sub>P structure.

Detailed structural studies of RAgGe for the heavy rare earth members were reported in refs. [11] and [12]. The R<sub>3</sub>Ag<sub>3</sub>Ge<sub>3</sub> structure can be viewed as alternating R<sub>3</sub>Ge and Ag<sub>3</sub>Ge<sub>2</sub> layers stacked along the  $c$  axis, shown as a  $c$ -axis projection in Fig. 1. In this structure there are three rare earth atoms in the hexagonal unit cell, sitting at  $3g$  sites with orthorhombic symmetry. Using

single crystal samples we have done a detailed analysis of temperature and field dependent anisotropic magnetization and transport measurements, and established the trends caused by the change of the rare earth in the physical properties. This has allowed us to more fully characterize the series than in the previous studies done on polycrystalline samples [12,13], and establish an experimental baseline for more detailed studies of specific members of this series.

In this paper we will present a brief review of experimental methods, followed by detailed experimental results of magnetization, magnetotransport and specific heat measurements for each compound. More attention will be paid to (i) YbAgGe, for which additional measurements down to 0.4 K were performed, and (ii) TmAgGe, for which an initial study of the in-plane anisotropy will be presented. The experimental section is followed by a brief discussion, where we will emphasize the observed trends in the magnetic properties within the series, as well as a few outstanding questions we are presently trying to address.

## 2 Experimental methods

Single crystals of RAgGe for R = Tb-Lu were grown from high temperature ternary solutions, rich in Ag and Ge [14,15,16]. Typical concentrations that resulted in good, well formed single crystals were  $R_x(\text{Ag}_{0.75}\text{Ge}_{0.25})_{1-x}$ , with  $x=0.06-0.14$ . This Ag-Ge rich self-flux was preferred not only because of the low-temperature, binary eutectic ( $\sim 650^\circ\text{C}$ ) around a Ag concentration of 75%, but also because it introduces no additional elements to the melt. The constituent elements were placed in an alumina crucible and sealed in a quartz ampoule under a partial pressure of Ar. After initially heating the ampoule to above  $\sim 1100^\circ\text{C}$ , it was slowly cooled to  $850-825^\circ\text{C}$ . After the slow cooling the excess solution was decanted and thin hexagonal rods, with the  $c$ -axis along the axis of the rod were obtained. Two noteworthy modifications to this growth procedure were YbAgGe which was cooled to  $750^\circ\text{C}$  before decanting and TbAgGe for which an initial melt stoichiometry of  $\text{Tb}_x(\text{Ag}_{0.85}\text{Ge}_{0.15})_{1-x}$  was necessary for better quality crystals. Fig. 2 shows a picture of an YbAgGe single crystal. Powder X-ray diffraction measurements were taken at room temperature with Cu  $K_\alpha$  radiation ( $\lambda = 1.5406 \text{ \AA}$ ) in order to confirm the crystal structure and to check for impurity phases. A typical pattern is shown in Fig. 3 for TmAgGe. There are no detectable second phase peaks and all of the detected ones can be indexed using a hexagonal structure with  $a=7.05(0.01) \text{ \AA}$  and  $c=4.14(0.01) \text{ \AA}$ . In Fig. 4, the volume and the dimensions of the unit cell across the series are shown as a function of the  $R^{3+}$  ionic radii [17], illustrating the expected lanthanide contraction. YbAgGe falls close to the monotonic decrease of the unit cell parameters, consistent with the Yb ion being essentially

trivalent at room temperature in this compound.

Attempts were made to grow even lighter rare earth members of this series (including YAgGe), both around and off the eutectic point of the Ag-Ge binary phase diagram. For R=Gd, we failed to grow the right phase when introducing rare earth amounts varying from 6% to as much as 37.5% into the  $\text{Ge}_{0.25}\text{Ag}_{0.75}$  melt; instead an initial composition of  $\text{Gd}_{0.06}(\text{Ge}_{0.25}\text{Ag}_{0.75})_{0.94}$  yielded orthorhombic crystals of  $\text{Gd}_3\text{Ag}_4\text{Ge}_4$ , space group *Immm* and lattice parameters, as given by single crystal structure determination,  $a=4.34 \text{ \AA}$ ,  $b=7.07 \text{ \AA}$  and  $c=14.49 \text{ \AA}$ . All the other compositions or R that we tried resulted in either no crystallization or crystals of as of yet unidentified phases.

The magnetization measurements on the RAgGe compounds that we are reporting here were performed in a Quantum Design MPMS SQUID magnetometer ( $T=1.8350\text{K}$ ,  $H_{max}=55$  or  $70\text{kG}$ ). We measured anisotropic magnetization for all compounds, having the external field  $H\parallel c$  or  $H\parallel ab$  (in a random *in-plane* orientation, unless otherwise specified), and the corresponding susceptibilities were then calculated as  $\chi = M/H$ ; the polycrystalline average susceptibility was evaluated as  $\chi_{ave} = (\chi_c + 2 * \chi_{ab})/3$ . We will infer the values of the transition temperatures (Néel temperature or spin reorientation temperatures) as determined from  $d(\chi * T)/dT$  [18] plots as well as from plots of  $C_p(T)$  and  $d\rho/dT$  [19]. YbAgGe is an exception and the criterion for determining its transition temperature will be discussed in the Yb section.

Additional measurements of the high field DC magnetization of TbAgGe were carried out with a vibrating sample magnetometer in a 180kG superconducting magnet (National High Magnetic Field Laboratory - Los Alamos Facility). For DyAgGe, HoAgGe and YbAgGe,  $M(H)$  measurements up to  $H=140\text{kG}$  were performed in a Quantum Design PPMS system using the extraction magnetization option. Most of the samples were manually aligned to measure magnetization along the desired axis, but for  $M(H, \theta)$  measurements in TmAgGe, the angular position of the sample was controlled by a modified MPMS sample rotor.

The electrical resistance in zero and applied field was measured with a Linear Research LR-700 AC resistance bridge ( $f=16\text{Hz}$ ,  $I=1-3\text{mA}$ ) in the magnetic field temperature environment of the QD MPMS system, using a standard four-probe technique. The current was flowing along the  $c$ -axis of the crystals. Due to the limitations imposed by the thin-rod shape of the samples, for axial ( $H\parallel c$ ) applied magnetic field, *longitudinal* ( $H\parallel I$ ) magnetoresistance was measured, whereas for magnetic field applied in the basal plane ( $H\parallel ab$ ), *transverse* ( $H \perp I$ ) magnetoresistance was studied. A  $^3\text{He}$  cooling system in the QD PPMS was used for measurements of the resistance of YbAgGe down to low temperatures ( $T=0.4\text{K}$ ). Given the geometry of the samples (partial or full hexagonal cross sections) and the orientation of the sample probe with

respect to the applied field, the field direction could in some cases be inferred to be  $H\parallel[120]$  (when using an orthogonal set of coordinates with  $a' = a$  and  $b' = a * \frac{\sqrt{3}}{2}$  while  $a$  is the hexagonal unit cell parameter). This will be discussed in further detail in the appropriate sections.

Heat capacity measurements were made in a Quantum Design PPMS system; in the cases of YbAgGe and LuAgGe, measurements down to  $T=0.4\text{K}$  were done using the  $^3\text{He}$  cooling option. The sample holder and grease background, measured separately for each sample, was later subtracted from the sample response. In order to estimate the magnetic contribution to the specific heat for the moment-bearing rare earth compounds, the specific heat of LuAgGe was subtracted. The magnetic part of the specific heat was used for the numerical integration of  $C_m(T)/T$  vs.  $T$ , which allowed us to estimate the temperature dependence of the magnetic entropy for each compound. The low temperature data (below actual measurements) for  $C_p(T)$  were estimated by non-linear fitting to (0,0) under the assumption that the small error thus introduced is further minimized by the subtraction of the Lu analogue.

### 3 Results

In presenting the data, we are characterizing each compound by magnetization, electrical resistivity and specific heat measurements. We will start with LuAgGe as the non-magnetic member of the series, and then progress from R=Tb through Yb. For each material and measurement that we present, we will try to emphasize properties that we find to persist in the series, as well as specific characteristics of each compound.

#### 3.1 LuAgGe

LuAgGe has electronic and magnetic properties consistent with a weakly diamagnetic intermetallic compound with no magnetic order. The magnetization as a function of temperature (Fig. 5a) is almost constant, with a very small, average, high temperature values around  $-2.3 \times 10^{-5}$  emu/mol ( $H\parallel ab$ ), and  $-3 \times 10^{-5}$  emu/mol ( $H\parallel c$ ) respectively. At low temperatures, an upturn in the susceptibility data occurs, which could be a consequence of some magnetic impurities being present in the original materials (*e.g.* the tail indicates a magnetic impurity contamination equivalent to 0.2% Gd). Field dependent magnetization curves for the two orientations of the field are shown in Fig. 5b; as expected for a non-magnetic compound with some magnetic impurities, the magnetization is a superposition of Brillouin saturation of the impurities with applied field, and a weak diamagnetic signal.

The temperature dependent resistivity of LuAgGe (Fig. 6) demonstrates the metallic character of this compound. Below  $\sim 50\text{K}$ , the impurity scattering becomes dominant, with a relatively large residual resistivity  $\rho(1.8\text{K}) \approx 45\mu\Omega\text{cm}$ , resulting in a relatively poor RRR of about 2, far smaller than the RRR values found in the rest of the series. The upper inset to Fig. 6 shows that there is no clear resistance minimum found in LuAgGe at low temperature. This is important to note given that for the R=Tb-Tm members of the RAgGe series do manifest a minimum in the temperature dependent resistivity for temperatures well above their respective Néel temperatures. The lower inset to Fig. 6 presents the transverse magnetoresistance, which varies approximately as  $H^2$ , as expected for normal metals.

Finally, we have measured the specific heat  $C_p$  as a function of temperature (Fig. 7). These data will be used as an estimate of the non-magnetic contribution to the specific heat in all RAgGe, R=Tb-Yb. As calculated from the linear fitting of the low-temperature  $C_p/T(T^2)$  data (Fig. 8), the electronic specific heat coefficient for the non-magnetic LuAgGe compound is:  $\gamma=(1.37\pm 0.02)$  mJ/mol\*K<sup>2</sup> whereas  $\Theta_D \approx 300$  K.

### 3.2 TbAgGe

The anisotropic, inverse susceptibility as a function of temperature for TbAgGe is shown in Fig. 9, together with the calculated polycrystalline average. The inset presents the low temperature region of the susceptibility for the applied field  $H=1\text{kG}$  parallel and perpendicular to the  $c$ -axis. The inverse susceptibility above  $\sim 50\text{K}$  is consistent with Curie-Weiss behavior of the magnetization:  $\chi(T) = C/(T + \Theta_P)$ , where  $\Theta_P$  is the paramagnetic Weiss temperature. The values of  $\Theta_P$  for the two orientations of the field, as well as for the polycrystalline average, are listed in Table 1 in the discussion section. A linear fitting of the average inverse susceptibility in the paramagnetic state gives a value of the effective moment  $\mu_{eff} = 9.7\mu_B$ , which is close to the theoretical value for  $\text{Tb}^{3+}$  of  $9.72\mu_B$ .

The low temperature susceptibility for  $H=1\text{kG}$  (shown as an inset in Fig. 9) indicates antiferromagnetic ordering below the Néel temperature  $T_N=28.4\text{K}$ . This transition temperature, as well as two others are seen more clearly for  $H\parallel c$  and can also be identified in the  $d(\chi T)/dT$  (around 28.5K, 24.7K and 19.8K respectively) and  $d\rho/dT$  (at 28.4K, 24.6K and 19.8K) (Fig. 10a and c); in  $C_p(T)$  (Fig. 10b) only the higher two transitions are visible, around 28.3K and 24.7K respectively. Another possible change in slope in  $M(T)/H$  occurs around 18K, but it is obscured in all other measurements, and is therefore unclear if it can be associated with another magnetic transition. However, in the  $H_c(T)$  phase diagram for  $H\parallel c$  (shown below), we can follow a phase

boundary indicative of such a transition.

Specific heat data was also used to estimate the magnetic entropy  $S_m(T)$ , shown in Fig. 10b, inset. From these data it can be inferred that the ordered state in TbAgGe is emerging out of triplet ground state, or there are at least a combination of a singlet and a doublet, or three singlet states closely spaced.

At high temperatures, the resistivity measurements (Fig. 11) indicate the metallic character of TbAgGe as  $\rho$  monotonically decreases with decreasing  $T$ . The residual resistivity ratio RRR, calculated as  $\rho(300K)/\rho(2K)$  and equal to 6.5, indicates fair crystal quality. The low temperature region of the resistivity measurements features slope changes associated with the magnetic transitions discussed above. On the other hand, there is a clear minimum of the  $\rho(T)$  curve around  $T \approx 50K$ . This minimum in resistivity occurs far above the Néel temperature (around  $2^*T_N$ ), which rules out the possibility of a superzone gap causing this feature, and, as will be seen below, occurs for all other local moment-bearing members of the series. This feature could be explained by magnetic fluctuations or some other, as of yet to be identified, mechanism.

Based on all the measurements performed on single crystals of TbAgGe, we can identify at least three transitions, at  $T=(28.4\pm 0.1)K$ ,  $(24.65\pm 0.05)K$  and  $(19.8\pm 0.1)K$ ; the lowest two temperatures are very close to those reported in [13] for the polycrystalline samples (from magnetization and neutron diffraction measurements) as the only transitions. We are thus led to believe that the highest (antiferromagnetic) transition temperature, as well as any other possible ordering temperatures, was not detected by the measurements made on polycrystalline samples.

Both resistivity (Fig. 12a) and magnetization measurements (Fig. 12b) as function of applied field provide evidence for a series of metamagnetic transitions in TbAgGe. Initial field dependent magnetization and resistivity measurements up to  $H=70kG$  reveal at least two metamagnetic transitions for critical fields  $H_c \approx 20kG$ , and  $48kG$  respectively, when field is applied along the  $c$ -axis. Given that the system seemed to be far below saturation ( $M(70kG) = 2.77\mu_B/Tb \ll 9\mu_B/Tb$ ), further magnetization measurements were performed for fields up to  $180kG$  and several other metamagnetic transitions were observed. (It should be noted that there is clear indication of hysteresis as manifested by the difference in  $M(H)$  for increasing and decreasing field measurements (inset, Fig. 12b)). The value of the magnetization at  $180kG$  is  $M = 7.78\mu_B/Tb$ , still below the calculated value for  $\mu_{sat}(Tb^{3+}) = 9.0\mu_B$ . This somewhat suppressed value of  $M$  could be consistent with more metamagnetic states beyond  $180kG$ , or with moments alignment at some angle  $\phi \neq 0$  with respect to the  $c$ -axis, or may simply be a caliper of the uncertainty in the absolute value of  $M$  in this high field measurement.

In order to better determine the number and extent of metamagnetic phases that exist for TbAgGe when  $H\parallel c$ , more measurements were done (Fig. 13a,b), which allowed us to plot a tentative  $H_c(T)$  phase diagram shown in Fig. 14. Local maxima of  $d(\chi T)/dT$  or  $dM/dH$  were used to estimate the  $H_c$  and  $T_c$  values, as illustrated in Fig. 13c. Numerous phases can be observed. Whereas figure 14 clearly shows the three,  $H = 0$ , transition temperatures discussed above, it also shows a lower field and temperature phase line existing for finite applied fields. Figure 13c illustrates that this lowest phase line is clearly detected in our  $M(T, H)$  data. A remaining question associated with this phase diagram is whether this lowest phase line intersects the  $H = 0$  axis at any finite temperature or flattens out at very low fields such that it intersects  $H = 0$  at  $T \approx 20$  K, where another transition already exists.

### 3.3 DyAgGe

Although DyAgGe in the paramagnetic state is more isotropic than TbAgGe, with slightly larger susceptibility for  $H\parallel c$  than for  $H\parallel ab$  (Fig. 15), it has an extremely anisotropic ordered state (as seen in Fig. 15a inset, for  $H=1$ kG); this low temperature anisotropy is further enhanced for lower (0.1kG) applied fields (Fig. 15b). Two transition temperatures are detected by  $d(\chi T)/dT$  (at 14.4 and 12.0 K),  $d\rho/dT$  (at 14.4K, and 12.0K) and  $C_p(T)$  (at 14.6K and 12.1K) (Fig. 16). These are in agreement with the temperatures determined by earlier measurements on polycrystalline samples [12,13]. There is one more, broader, lower temperature peak in Fig. 16a, not visible in any other measurement. But comparison of  $d(\chi T)/dT$  plots for two different applied fields (Fig. 16a,  $H=0.1$ kG and  $H=1$ kG) seems to indicate that the low temperature peak is moving down in  $T$  rapidly as the applied field increases, whereas the other two are unaffected by the change in  $H$ . In order to examine the low temperature state of DyAgGe more carefully 0.1 kG zero-field-cooled-warming (ZFC) and field-cooled warming (FC) data sets were taken and are plotted in Fig. 17. These data are consistent with an ordered state below 12.0 K that has a net ferromagnetic component along the  $c$ -axis. The broadness and the field sensitivity of the lowest temperature peak in Fig. 16a, as well as the difference between the ZFC and FC data sets shown in Fig. 17 are consistent with the rotation of domains in small applied fields. It should also be noted that the magnetization associated with the lowest temperature point of the FC curve shown in Fig. 17 corresponds to  $M \sim 0.66\mu_B/\text{Dy}$ , the value associated with the low field plateau of the  $M(H)$  plot shown in Fig. 18. This further supports the idea that below  $T \sim 12$  K the magnetically ordered state of DyAgGe has a net ferromagnetic component along the  $c$ -axis.

The linear behavior of the inverse susceptibility above  $\sim 50$ K (Fig. 15a) is indicative of Curie-Weiss like susceptibility, the effective magnetic moment



determined from the linear region being  $\mu_{eff} = 10.3\mu_B$  (in good agreement with the theoretical value for  $\text{Dy}^{3+}$ , which is  $10.6\mu_B$ ). Paramagnetic Weiss temperatures  $\Theta_P$  are listed in Table 1.

The resistance of DyAgGe increases linearly with temperature above 50K (Fig. 19). At low temperatures, the resistivity has a local minimum around 30K, followed by a sharp drop around the transition temperature; this indicates loss of spin disorder scattering as the system enters the ordered state. The residual resistivity ratio RRR is approximately 5.2.

Field dependent magnetization measurements indicate a complex metamagnetism in DyAgGe, as shown in Fig. 18: transitions can be seen in all three orientations of the applied field ( $H\parallel[001]$ ,  $H\parallel[120]$  and  $H\parallel[010]$ ), which probably means that, in the saturated state, the magnetic moments are inclined at some angle  $0^\circ < \varphi < 90^\circ$  with respect to the  $c$ -axis. This could justify the low magnetization values (below the theoretical value  $\mu_{sat}(\text{Dy}^{3+}) = 10\mu_B$ ) in all three directions even at the highest applied field, as we explain in more detail in the discussion section.

The critical fields for the metamagnetic transitions are  $H_c \approx 14\text{kG}$ ,  $31\text{kG}$ ,  $45\text{kG}$  for  $H\parallel[120]$ ,  $13\text{kG}$ ,  $31\text{kG}$ ,  $60\text{kG}$  for  $H\parallel[010]$ , and  $3\text{kG}$ ,  $12\text{kG}$ ,  $46\text{kG}$ ,  $50\text{kG}$ ,  $71\text{kG}$  for  $H\parallel c$  respectively where it should be noted that for  $H\parallel c \sim 3\text{ kG}$  the transition is thought to be associated with domain rotation (as discussed above). These values can also be seen in the  $R(H)$  curves, shown in Fig. 20 for  $H\parallel c$  and  $H \perp c$ , except for the ones beyond  $55\text{kG}$ , which was the upper field limit for this magnetoresistance measurement. Once metamagnetism of planar moments is better understood (see discussion section on metamagnetism in TmAgGe below) the study of the angular dependence of metamagnetism in DyAgGe, a system with highly anisotropic but non-planar, non-axial moments, should be interesting and hopefully tractable.

### 3.4 HoAgGe

The susceptibility of HoAgGe in the paramagnetic state is almost isotropic, as can be seen in Fig. 21. For temperatures higher than 50K the susceptibility follows the Curie-Weiss law  $\chi(T) = C/(T + \Theta_P)$ ; the corresponding paramagnetic temperatures  $\Theta_P$  are given in Table 1. From the linear fit of the inverse susceptibility (for the polycrystalline average) we get an effective moment  $\mu_{eff} = 10.0\mu_B$ , close to the theoretical value  $\mu_{eff}(\text{Ho}^{3+}) = 10.6\mu_B$ . The compound orders antiferromagnetically below Néel temperature  $T_N=11.0\text{K}$ , whereas a spin reorientation transition occurs around  $T=7.4\text{K}$ . Although  $T_N$  shows up as a sharp, well-defined peak in all three plots in Fig. 22, the lower transition temperature is indicated by broader peaks in  $d(\chi T)/dT$  around  $7.4\text{K}$

(Fig. 22a), and in  $d\rho/dT$  around 8.0K (Fig. 22c); specific heat plot shown in Fig. 22b seems to have an even broader feature close to these temperatures. It should be noted that, as in the case of TbAgGe, the measurements on polycrystalline samples [13] missed a transition (*e.g.* the lower one for HoAgGe), whereas the reported temperature of the upper transition falls close to our measured value.

The temperature dependent resistivity measurement (Fig. 23) demonstrates the metallic character of this compound and the residual resistivity ratio for HoAgGe is RRR=4.0. At a temperature of about 19K a broad minimum in  $\rho(T)$  is observed, and a drop in resistivity due to the loss of spin disorder scattering in the magnetically ordered phase.

From the specific heat measurements shown in Fig. 22b we calculated the magnetic entropy  $S_m$  of this compound (shown in the inset); the value of the entropy,  $S_m \approx R \ln 4$ , at the change in slope that occurs around the ordering temperature suggests that the magnetic order in HoAgGe emerges out of state with a degeneracy of 4.

The magnetization curves as a function of applied field (Fig. 24a) reveal a series of metamagnetic transitions for  $H$  applied in the  $ab$ -plane, with critical field values of around 11.0kG, 22.0kG and 35.0kG for  $H\parallel[010]$ , and 12.0kG, 23.0kG and 28.0kG respectively for  $H\parallel[120]$ , whereas when  $H$  is applied along the  $c$ -axis the magnetization curve can either be a broad metamagnetic transition or a continuous spin-flop transition. The theoretical value of the saturated magnetization expected for  $\text{Ho}^{3+}$  ( $\mu_{sat} = 10\mu_B$ ) is not reached by fields up to 140kG in any of the three orientations; as mentioned before, this can be due to the moments being along an inclined axis with respect to the  $c$ -axis of the crystals, or further support the idea of the spin-flop transition, especially given the continuous increase in magnetization as  $H$  is being increased. Another possible explanation, which we detail for TmAgGe, is related to the crystal structure of these compounds and will be discussed below.

We have also measured magnetoresistance for  $H\parallel ab$  (Fig. 24b), and it is consistent with the various metamagnetic states seen in  $M(H)$ . Given the geometry of the crystals, there was more uncertainty in orienting the resistance pieces than the ones for magnetization measurements; consequently, we can infer the approximate orientation of the field in the magnetoresistance measurement by comparison of these data with the  $M(H)$  curves for  $H\parallel ab$ : since various features in  $\Delta\rho(H)/\rho(0)$  occur close to the critical fields in  $M([120])$  (Fig. 24b), it seems that  $H$  was almost parallel to the  $[120]$  direction.

### 3.5 ErAgGe

So far in the RAgGe series, we have seen a progression from axial anisotropy in TbAgGe toward  $M_{ab} \sim M_c$  for HoAgGe. ErAgGe continues this trend with the local Er moments becoming far more planar in nature (Fig. 25). This is analogous to the trend seen in many tetragonal systems [1,2], in which the change in sign of the  $B_{20}$  CEF parameter causes a switch from planar to axial moments between Ho and Er [20,21].

The inverse susceptibility of ErAgGe is linear above 75K, with  $\mu_{eff} = 9.3\mu_B$ , fairly close to the theoretical value of  $9.6\mu_B$  for  $\text{Er}^{3+}$ . The anisotropic Weiss temperatures  $\Theta_P$  are given in Table 1. For a 1kG field applied parallel to the  $ab$ -plane, magnetic ordering is observed below 3K (inset, Fig. 25); a smaller feature seems to indicate the same ordering temperature for field applied parallel to the  $c$ -axis.

The temperature dependent resistivity is consistent with local moment ordering and manifests a local maximum in  $d\rho/dT$  at 3K (Fig. 26c). Below the ordering temperature a decrease in resistivity (Fig. 27) corresponds to the loss of spin-disorder scattering, as the magnetic moments become antiferromagnetically ordered. The high temperature resistivity is typical of intermetallic compounds, increasing up to  $\sim 100\mu\Omega cm$  at  $T=300\text{K}$ , and leading to a RRR value of  $\sim 3.0$ . The increasingly ubiquitous local minimum in the resistivity can still be observed above  $T_N$ , centered near  $T \sim 6$  K. In Fig. 26b the specific heat shows a well-defined peak at  $T \approx 3.2\text{K}$ , very close to the temperature of the maximum in  $d(\chi T)/dT$  (Fig. 26a). The inset is a plot of the magnetic entropy of ErAgGe, where the break in slope around  $S_m \approx R \ln 2$  indicates that the ground state of this compound is a Kramers doublet.

In the  $M(H)$  plots (Fig. 28a) we again see clear anisotropy, with the moments somewhat constrained to the basal plane. For field applied along the  $c$  direction, magnetization linearly increases with field, up to  $H \approx 50\text{kG}$ ; right before the maximum applied field  $H=55\text{kG}$ , an upturn in the  $M(H)$  curve is apparent, possibly indicating a subsequent metamagnetic transition. When field is applied parallel to the  $ab$ -plane, we see a broad, poorly defined metamagnetic transition, as our measurements are being taken at  $T=2\text{K}$ , close to  $T_N$  of this compound. The magnetoresistance for  $H\parallel ab$  (Fig. 28b) shows a local maximum around  $H=11\text{kG}$ , which further indicates the presence of a metamagnetic transition for this critical field.

### 3.6 TmAgGe

Magnetization measurements with field applied perpendicular and parallel to the  $c$ -axis (Fig. 29) indicate extreme anisotropy in TmAgGe:  $\chi_{ab}/\chi_c \approx 30$  at  $T=5.0\text{K}$ . This temperature was chosen just above the antiferromagnetic ordering temperature  $T_N \approx 4.2\text{K}$ . Above  $\sim 100\text{K}$ , inverse susceptibilities are linear with  $\mu_{eff} = 7.9\mu_B$ , close to the theoretical value of  $\mu_{eff}(\text{Tm}^{3+}) = 7.6\mu_B$ .

Figure 30 shows a sharp peak in  $C_p(T)$  as well as  $d(\chi T)/dT$  for  $4.2 \pm 0.1\text{K}$ . The zero-field resistivity data shown in Fig. 31, supports the ordering temperature inferred from the thermodynamic data. The plot of  $d\rho/dT$  (Fig. 30c) has a clear peak between 4.0 and 4.6 K. In the inset of Fig. 30b, the calculated magnetic entropy  $S_m(T)$  has a break in slope close the transition temperature  $T_N$ , for an entropy value of  $\sim R \ln 2$ , indicative of a doublet ground state or two closely spaced singlets. Below  $T_N$ , loss of spin disorder scattering is apparent from the sudden drop in resistivity, due to the antiferromagnetic ordering of the  $\text{Tm}^{3+}$  moments. Above the ordered state, the resistance goes through a broad local minimum around 15K (far higher than  $T_N$ ), after which it starts increasing; for temperatures higher than  $\sim 100\text{K}$  it becomes approximately linear. The residual resistivity ratio  $\text{RRR} \approx 4.0$  reflects acceptable quality of these crystals.

Clear metamagnetism is seen in the  $M(H)$  plot in Fig. 32a for in-plane field orientation, as well as in magnetoresistance measurements shown in Fig. 32b. Below  $H=70\text{kG}$ , the in-plane magnetization curves in Fig. 32a show two metamagnetic transitions for  $H\parallel[120]$ , with critical field values  $H_{c1} \approx 4.25\text{kG}$  and  $H_{c2} \approx 9.25\text{kG}$ ; for the other orientation,  $H\parallel[010]$ , they merge into a single transition with a critical field around  $H_c \approx 6.0\text{kG}$ . A very complex angular dependence of the critical fields, as well as of the locally saturated magnetization values, can thus be anticipated; this is subject of a separate, more detailed study [22].

Similar to the case of HoAgGe, we compare the position of any features revealed by the magnetoresistance measurement in Fig. 32b to the critical field values that we get from  $M(H\parallel ab)$  curves. Below 10kG, there is one obvious peak, and another possible change of slope in the plot in Fig. 32b; therefore we could probably assume that the field was close to the  $[120]$  direction, for which two metamagnetic transitions can be seen in  $M(H)$ . However, there is another broad peak in the magnetoresistance that can not be correlated with any feature in magnetization, and which requires further investigation.

### 3.7 YbAgGe

YbAgGe is a compound with some distinctly different properties compared to all previous members of the series. Fig. 33 shows the inverse anisotropic susceptibility in an applied field  $H=1\text{kG}$ . It is linear above  $\sim 20\text{K}$ , indicating Curie-Weiss behavior at high temperatures with an effective moment of  $\sim 4.4\mu_B/\text{Yb}$ ; however, below this temperature, as can be seen in the inset from low temperature susceptibility, there is no sign of magnetic ordering down to  $1.85\text{K}$ . Instead there is an apparent loss of local moment behavior, manifesting itself as a levelling off of the susceptibility. Also, no distinct features appear in the  $M(H)$  or magnetoresistance data at  $T=2\text{K}$  (Fig. 34a,b): for  $H\parallel c$  magnetization linearly increases with  $H$  up to  $H=140\text{kG}$ , whereas the in-plane data show that the compound is probably approaching saturation (the fact that the high field magnetization is lower than calculated  $\mu_{sat}(\text{Yb}^{3+}) = 4.0\mu_B$  is possibly a result of the crystal structure and CEF anisotropy of the RAgGe series, see the discussion below); magnetoresistance at this temperature is consistent with what one would expect for anisotropic, paramagnetic metal.

As can be seen in Fig. 35a, no significant change occurred after annealing ( $600^\circ\text{C}$  for 1 week), and the RRR increase (from 2.8 up to 3.1) was slight. The annealing temperature was limited by the possibility of melting the small amount of residual flux on the sample (note the Ag-Ge eutectic at  $\sim 650^\circ\text{C}$ ). The temperature dependences of the resistivity, and the specific heat (shown below) were almost identical before and after the heat treatment of the crystals.

On the other hand the temperature dependent electrical resistivity can be changed significantly by the application of magnetic field. When large field is applied (Fig. 35b), there is an increase in the RRR value: for  $H\parallel ab$ , the RRR value increases dramatically to  $\text{RRR} \sim 10$ . This indicates that crystal purity is quite high and apparently the large residual resistivity  $\rho_0$  for  $H=0$  is due to sensitivity of hybridized Yb state to relatively minor disorder.

In order to characterize this compound at lower temperatures we have to rely on the resistivity (Figs. 35 and 36) and specific heat (Figs. 36 and 37) measurements which were taken down to  $0.4\text{K}$ . (Due to the limitations imposed by our measurement systems magnetization data only go down to  $1.85\text{K}$ .) As the sample is cooled below  $1.8\text{K}$  there are two features visible in both the resistivity and specific heat. At  $1.0\text{K}$  there is a slight but clear change in slope of the resistivity and there is a relatively broad maximum in the specific heat. At  $0.65\text{K}$  there is an extremely sharp drop in resistivity and as well as a sharp peak in the specific heat. Specific heat data were taken upon heating as well as cooling of the sample (Fig. 36b, inset) indicating that if there is any hysteresis associated with the  $0.65\text{K}$  transition it is smaller than the peak

width.

The calculated magnetic entropy  $S_m$  (Fig. 38) at  $T = 1.0$  K is significantly less than  $R \ln 2$ . Based on this we can assume that the transition corresponds to small magnetic moment ordering. This is in agreement with the enhanced electronic specific heat coefficient  $\gamma \geq 154$  mJ/mol K<sup>2</sup> that we get from extrapolation of the high temperature part of the  $C_p/T$  vs.  $T^2$  (Fig. 37) to  $T^2=0$ .

Low temperature small magnetic moment ordering is not the only feature indicating that YbAgGe is probably a heavy Fermion compound: deviations from the Curie-Weiss behavior in  $\chi_{ave}$  (for which CEF effects are cancelled to the first order) below  $\sim 20$  K, and quite large Weiss temperature ( $\Theta_{ave} \approx -30$  K) suggest that Yb 4*f* levels may be significantly hybridized. If this is true, an estimate of the Kondo temperature is given by  $\Theta/10 \leq T_K \leq \Theta$  [23], i.e.  $3\text{K} \leq T_K \leq 30\text{K}$ . Specific heat data plotted as  $C_p/T$  vs.  $T^2$  (Fig. 37) reveal a distinct enhancement of the electronic specific heat coefficient (compared with the data for LuAgGe on the same plot). This  $\gamma \sim 150$  mJ/mol K<sup>2</sup> value, already being significantly enhanced by itself, is apparently a lower limit of  $\gamma$  since a significant upturn in  $C_p/T$  vs.  $T^2$  is observed below approximately 10K, similar to that seen in many heavy fermion compounds [24], including for example YbNi<sub>2</sub>B<sub>2</sub>C [25] and YbRh<sub>2</sub>Si<sub>2</sub> [26]. Keeping in mind that YbAgGe has a low temperature magnetic ordering, and that therefore an ambiguity in the evaluation of low temperature electronic specific heat coefficient is present, Fig. 37 suggests that low temperature  $\gamma$  is within the range of  $\sim 150$  mJ/mol K<sup>2</sup> to 1 J/mol K<sup>2</sup>. This crude estimate allows us to classify YbAgGe as a new Yb heavy fermion compound, with low temperature reduced moment magnetic ordering, which we already reported in [27]. Using the single impurity relation [24], we can estimate the Kondo temperature as  $T_K = w_N \pi^3 R / 6\gamma$ , where  $w_N=0.4107$  is the Wilson number and  $R$  is the gas constant. Using the aforementioned range of the value of  $\gamma$ , the Kondo temperature can be evaluated as  $15 \text{ K} < T_K < 120 \text{ K}$ . Additionally, we can estimate the Wilson ratio,  $\mathcal{R} = 4\chi\pi^2 k_B^2 / 3\gamma\mu_{eff}^2$  [24] for YbAgGe using  $\chi$  and  $\gamma$  determined at  $T = 1.8$  K, and the high temperature effective moment  $\mu_{eff}$ , as  $\mathcal{R} \approx 1.8$ , which is close to  $\mathcal{R} = 2$  expected for heavy fermion compounds, and much higher than  $\mathcal{R} = 1$ , the Wilson ratio for non-interacting electrons [24].

Having a Néel temperature, apparently associated with small moment ordering, so close to  $T=0\text{K}$  makes YbAgGe an interesting system for the study of the competition between magnetically ordered and correlated ground state. It is anticipated that pressure should be a possible parameter for stabilizing the antiferromagnetic ground state.

While preparing this manuscript for publication, a very recent report on the heavy fermion character in YbAgGe came to our attention [28]. Although these authors did not go to low enough temperatures to detect the ordering

Table 1

Magnetic ordering temperatures,  $T_m$ , effective magnetic moments and anisotropic paramagnetic Weiss temperatures  $\Theta_p$ .

	Tb	Dy	Ho	Er	Tm	Yb
$T_m(\text{K})$	28.4±0.1,	14.5±0.1,	11.0±0.2,			0.95±0.05,
	24.6±0.1,	12.15±0.1	7.7±0.1	3.1±0.1	4.15±0.1	0.65±0.05
	19.8±0.1					
$\mu_{eff}(\mu_B/\text{R})$	9.7	10.4	10.0	9.3	7.9	4.4
$\Theta_{ab}(\text{K})$	-53.8	-25.5	-10.1	-3.6	7.5	-15.1
$\Theta_c(\text{K})$	1.0	7.4	-1.9	-36.4	-76.3	-83.5
$\Theta_{ave}(\text{K})$	-28.3	-10.5	-7.1	-10.9	-14.4	-30.1

below 1 K, their other data is in good agreement with what we have presented here and elsewhere [27].

#### 4 Discussion

Among many properties that we see in the RAgGe series, anisotropy and metamagnetism are particularly interesting, specifically in light of the crystal structure of these compounds: a hexagonal unit cell with a single rare earth site of orthorhombic point symmetry. Across the series, the magnetization is anisotropic, going from axial (in TbAgGe) to extreme planar (in TmAgGe). The magnetic and transport properties throughout the RAgGe series proved to be anisotropic, due primarily to the CEF splitting of the Hund's rule ground state multiplet. In Table 1 the Weiss paramagnetic temperatures are given, for the two orientations of the field, as well as for the polycrystalline average. Negative values for  $\Theta_{ave}$  for all R suggest antiferromagnetic interactions between magnetic moments, although Dy may be an exception, given the presence of the small ferromagnetic component of the magnetization. TbAgGe has an easy axis parallel to  $c$  in the paramagnetic state. This is followed by a progression towards a more isotropic case (R=Ho) while having  $\Theta_{ab} < \Theta_c$ , whereas for R=Er-Yb the easy axis lies in the  $ab$ -plane and  $\Theta_{ab} > \Theta_c$ . The analysis of this anisotropy should allow for the determination of the leading term in the crystal field Hamiltonian, similar to the case of tetragonal systems. But a more complex calculation is needed for our hexagonal compounds, where the R ions are located at sites with *orthorhombic* point symmetry, and this is beyond the scope of the current paper.

The ordering temperatures in RAgGe (R=Tb-Tm) approximately scale with the de Gennes factor  $dG = (g_J - 1)^2 J(J + 1)$  (Fig. 39), where  $g_J$  is the Landé  $g$

factor and  $J$  is the total angular momentum of the  $R^{3+}$  ion Hunds rule ground state. This is consistent with the coupling between the conduction electrons and the local magnetic moments giving rise to the long range magnetic order via the RKKY interaction. However, significant deviations from the linearity may be noticed, suggesting other factors may be involved (i.e. strong CEF effects constraining the moments to either the  $ab$  plane or the  $c$  axis, as seen in the already mentioned tetragonal compounds [1,2,29]).

Because the strong CEF splitting confines the magnetic moments to the basal plane in TmAgGe this compound is the simplest candidate in this series for a study of the metamagnetism.  $Tm^{3+}$  ions occupy  $3g$  Wyckoff sites, with  $m2m$  (*orthorhombic*) point symmetry, leading to a hexagonal structure with three R ions per unit cell (Fig. 1). Consequently, referring to a single unit cell, we can assume that the magnetic moments of the three R ions behave like Ising systems, rotated by  $120^\circ$  with respect to each other in the basal plane. The saturated state is reached when the three magnetic moment vectors add constructively (Fig. 40).

To further examine the extreme basal plane anisotropy, we measured  $M(\theta)$  for an applied field  $H=70\text{kG}$  parallel to the  $ab$  plane (Fig. 41), where  $\theta$  is the angle between the direction of the field and one of the high symmetry directions. Not only is the magnetization angular dependent, but also it displays a *6-fold* symmetry, consistent with the hexagonal unit cell. The maxima in the angular dependent magnetization occur for  $\theta = (2n + 1) * 30^\circ$  ( $n$ -integer), when angle  $\theta$  is measured from the  $[010]$  orthogonal axis. As a consequence, within our model with a superposition of three Ising systems, for the saturated state we can assume the magnetic moments configuration shown in Fig. 40.

Using Fig. 40, we can evaluate the expected values of the longitudinal magnetization (the quantity we measure) in the saturated state, for two different orientations of the applied field: when  $H \parallel [120]$ ,

$$\begin{aligned} M(H \parallel [120]) &= \frac{1}{3} [\mu_{sat}(Tm^{3+}) + 2\mu_{sat}(Tm^{3+}) \cos 60^\circ] = \\ &= \frac{1}{3} [\mu_{sat}(Tm^{3+}) + 2\mu_{sat}(Tm^{3+}) * \frac{1}{2}] = \\ &= \frac{2}{3} \mu_{sat}(Tm^{3+}) = \frac{2}{3} * 7.0\mu_B = 4.67\mu_B \end{aligned}$$

For the other *in-plane*, orthogonal direction ( $H \parallel [010]$ ), we get

$$M(H \parallel [010]) = \frac{1}{3} [0 + 2\mu_{sat}(Tm^{3+}) \cos 30^\circ] =$$



$$\begin{aligned}
&= \frac{2}{3} \mu_{sat}(Tm^{3+}) \cos 30^\circ = \\
&= \frac{2\sqrt{3}}{3} \frac{\mu_{sat}(Tm^{3+})}{2} = \frac{2\sqrt{3}}{3} \frac{7.0\mu_B}{2} = 4.04\mu_B
\end{aligned}$$

This results in a calculated ratio

$$\left. \frac{M(H\parallel[010])}{M(H\parallel[120])} \right|_{calc} = \cos 30^\circ = \frac{\sqrt{3}}{2} = \frac{4.04}{4.67} = 0.867$$

If we compare these model calculations with the two corresponding measured values from  $M(\theta)$  in Fig. 41, we notice that

$$\left. \frac{M(H\parallel[010])}{M(H\parallel[120])} \right|_{exp} = \frac{M(\theta = 0^\circ)}{M(\theta = 30^\circ)} = \frac{0.0447}{0.0551} = 0.875$$

is close to the anticipated value. Together with the experimental, angular dependent magnetization (open circles), Fig. 41 also shows the angular dependence of  $M$  (solid line), calculated based on the above model for  $\theta = 120-180^\circ$ . The small, yet noticeable, deviations of the cosine function from the measured data could have been caused by slight misalignment of the extremely small sample used for the rotation measurements; as a result, the rotation axis makes a small angle with the  $ab$ -plane, resulting in a weak 2-fold modulation of the of  $M(\theta)$ , yielding the asymmetric experimental peaks.

In Fig. 32, above  $\sim 15$ kG we see a wide plateau in magnetization for the two high symmetry orientations; the corresponding magnetization values, even at highest applied field,  $H=70$ kG, are  $M(H\parallel[120]) = 4.92\mu_B$ , and  $M(H\parallel[010]) = 4.30\mu_B$ , far below  $\mu_{sat}(Tm^{3+}) = 7\mu_B$ . Instead of attributing this to additional metamagnetic transitions beyond 70kG, we notice that the magnetization values for the corresponding orientations of the field, and their ratio:

$$\left. \frac{M(H\parallel[010])}{M(H\parallel[120])} \right|_{exp} = \frac{4.30}{4.92} = 0.875$$

are consistent with our model. As the above ratio is close to the expected  $\cos 30^\circ$  value, the absolute values of the magnetization are  $4.30\mu_B$  and  $4.92\mu_B$ , both larger than the corresponding values within our model (i.e.  $4.04\mu_B$ , and  $4.67\mu_B$  respectively). However, the extrapolations of the high-field plateaus down to  $H=0$  (straight lines in Fig. 32a) intersect the magnetization axis at  $4.0\mu_B$  and  $4.63\mu_B$ , very close to the anticipated theoretical values. This could

be further indication of the validity of our model applied to this compound, while the slow increase in magnetization above alleged saturation could indicate a slow approach of the CEF splitting energy.

The model in which we assume three Ising systems  $120^\circ$  apart in the  $ab$ -plane of a hexagonal unit cell, seems to describe well the metamagnetism in TmAgGe; furthermore, it can be used to describe at least one more compound isotopic to TmAgGe (*i.e.* TbPtIn), and it will be used for a study of the angular dependent metamagnetism in the two systems in a detailed paper yet to come [22].

If we release the restriction that the three Ising systems be planar, while still imposing that their in-plane projections be  $120^\circ$  apart to agree with the symmetry of the crystals, we find this modified model can describe the case of DyAgGe quite well. From the crystal structure of this compound, and the orthorhombic symmetry of the rare earth sites, we can assume that the three R magnetic moments of the unit cell align themselves along three non-planar equivalent directions. We notice that for  $H=140\text{kG}$  (Fig. 18), the ratio of the magnetizations for the two in-plane orientations (when  $H$  is parallel to the two independent high symmetry axes) is:

$$\frac{M(H\parallel[120])}{M(H\parallel[010])}\Big|_{exp} = \frac{4.02}{4.51} = 0.89$$

This is close to the previously calculated value of for the planar model assumed for TmAgGe. In the case of DyAgGe, given that the three  $M(H)$  curves in Fig. 18 seem to indicate that the moments are tilted outside the  $ab$ -plane, a model similar to that used for TmAgGe, enhanced to 3 dimensions, may be appropriate. Let us assume that the three  $\text{Dy}^{3+}$  magnetic moments lie on a cone around the  $c$ -axis, with the projections in the  $ab$  plane  $120^\circ$  apart from each other. These in-plane projections will then behave similarly to the full moments in the case of  $\text{Tm}^{3+}$ , and thus  $M(H\parallel[010])$  represents  $\frac{2}{3}$  of the total  $ab$  magnetization  $M_{ab}$  (if we assume saturation at  $H=140\text{kG}$ ):  $M(H\parallel[010]) = \frac{2}{3}M_{ab}$ . Then  $M_{ab} = \frac{3}{2}M(H\parallel[010]) = \frac{3}{2} * 4.51\mu_B = 6.77\mu_B$ . Together with the axial component  $M_c(\equiv M(H\parallel[001])) = 6.85\mu_B$ , we can now estimate the total magnetization at  $H=140\text{kG}$ :  $M(140\text{kG}) = \sqrt{(6.77\mu_B)^2 + (6.85\mu_B)^2} \approx 9.63\mu_B$ , close enough to the calculated value  $\mu_{sat}(\text{Dy}^{3+}) = 10\mu_B$ . We conclude that the model we assumed for the magnetic moments is consistent with the experiment. Moreover, one can estimate the angle  $\varphi$  of the saturated magnetization with respect to the  $c$ -axis: from the in-plane magnetization being along the  $[010]$  direction, we can conclude that, in the saturated state, the total magnetization vector lies along a  $[0kl]$  axis. The angle  $\varphi$  with the  $c$ -axis can be calculated as:  $\tan \varphi = \frac{M_{ab}}{M_c} = \frac{6.77}{6.85} = 0.99$  and thus  $\varphi \approx 45^\circ$ .

The lattice parameters of the hexagonal unit cell in DyAgGe are given in Fig. 4 to be  $a = 7.09\text{\AA}$  and  $c = 4.20\text{\AA}$ ; in the orthogonal system of coordinates that we use in defining the crystalline directions, these correspond to  $a' = a = 7.09\text{\AA}$ ,  $b' = a * \frac{\sqrt{3}}{2} = 6.14\text{\AA}$  and  $c' = c = 4.20\text{\AA}$ . We can now write the direction given by the angle  $\varphi$  in terms of Miller indices  $h$ ,  $k$  and  $l$ , where  $h = 0$ , and  $k$  and  $l$  are such that

$$\tan \varphi = 0.99 = \frac{kb'}{lc'} = 1.46 \frac{k}{l} \Rightarrow \frac{k}{l} = 0.68$$

The closest integer values for  $k$  and  $l$  are thus 2 and 3 respectively, which means that in DyAgGe the saturated magnetization vector  $M$  is parallel to the  $[023]$  direction.

HoAgGe resembles DyAgGe in that both these compounds show metamagnetic transitions for both high-symmetry directions in the  $ab$ -plane. However attempts to apply the Dy model to Ho failed because the in-plane magnetization is almost isotropic in HoAgGe (Fig. 24a), with

$$\frac{M(H\|[120])}{M(H\|[010])}\Big|_{exp} = \frac{6.01}{6.14} = 0.98 \gg 0.89 = \frac{\sqrt{3}}{2}$$

Another important observation is that in DyAgGe, the last seen metamagnetic transition is followed by an almost constant magnetization (wide plateaus in all three orientations of the field), supportive of the idea of a stable saturated state above  $\sim 80\text{kG}$ ; in HoAgGe however, magnetization keeps increasing with the applied field, possibly indicating a continuous spin-flop transition, as already mentioned. If this is true, than with fields around  $100\text{kG}$  this compound is already in a regime of weak CEF, therefore any variant of the previous model is inappropriate. It is worth noting though that HoAgGe is rather curious given its anisotropy (clear metamagnetism in the two in-plane directions and no clear transition for  $H\|c$ ). At some future date it would be interesting to study the angular dependence of metamagnetism in DyAgGe and HoAgGe, to see how the phase diagrams vary as the anisotropy is being relaxed.

Insufficient data on ErAgGe (i.e. two in-plane orientations, higher fields) as well as the low  $T_N$  and the single, rather broad feature in  $M(H)$  prevent us from checking how the model applies to this compound.

All RAgGe described here seem to be good metals, as shown by the monotonic increase of the resistivity at high temperatures; the residual resistivity ratio RRR ranges from 2.0 to 6.5, and it did not seem to improve considerably by annealing in the case of YbAgGe. However it should be noted that YbAgGe

has a RRR of about 10 in a 140kG applied field, significantly larger than that without field, indicating that a lot of the scattering in this compound is magnetic in origin.

All of the magnetically ordered compounds in this study, except for YbAgGe, have a rather unusual, pronounced minimum in the temperature dependent resistivity above the magnetic transition. It is similar to the  $\rho(T)$  behavior recently found in a different family, RCuAs<sub>2</sub> (for R=Sm, Gd, Tb, Dy) [30]. It has to be seen if this type of behavior indeed requires, as suggested in [30], novel ideas for electrical transport phenomena in the paramagnetic state of relatively simple magnetic metals, but the mere fact that similar, atypical, temperature dependence is observed in resistivity of the members of two unrelated families, RCuAs<sub>2</sub> and RAgGe, in the latter case in single crystals, certainly asks for some theoretical input as well as search for other examples.

YbAgGe appears to be a very promising example of a Yb-based intermetallic compound with clear hybridization. Whereas it does not order magnetically within our  $M(T)$  measurement range (above 1.85K), it does have a clear small moment ordering below 1.0 K and also has an enhanced electronic specific heat coefficient value ( $\gamma > 150$  mJ/mol\*K<sup>2</sup>). Based on these data we can conclude that YbAgGe is a heavy fermion, with small moment ordering at very low temperature. Consequently, there is a possibility of approaching a quantum critical point by experiments under applied magnetic field, variable pressure, or with changing lattice parameters with doping, or with variable concentration of the magnetic moments (i.e. of the Yb<sup>3+</sup> ions). While in an isotropic case, application of pressure in Yb compounds close to quantum critical point is expected to increase the ordering temperature [31], crystallographically and electronically anisotropic materials like YbAgGe may have non-trivial response to pressure. More investigation is needed for a better understanding of the nature of the ordering in YbAgGe.

*Acknowledgments:* We would like to thank Cedomir Petrovic and Raquel Ribeiro for help with powder X-ray diffraction and Cathie Condon for single crystal X-ray analysis of Gd<sub>3</sub>Ag<sub>4</sub>Ge<sub>4</sub>. Ames Laboratory is operated for the U.S. Department of Energy by Iowa State University under Contract No. W-7405-Eng.-82. This work was supported by the Director for Energy Research, Office of Basic Energy Sciences. Work at NHMFL - Los Alamos Facility was performed under auspices of the National Science Foundation and the U.S. Department of Energy.

## References

- [1] K.D.Myers, S.L.Bud'ko, I.R.Fisher, Z.Islam, H.Kleinke, A.H.Lacerda and P.C.Canfield, *J. Magn. Magn. Mater.*, **205** (1999) 27.
- [2] S.L.Bud'ko, Z.Islam, T.A.Wiener, I.R.Fisher, A.H.Lacerda and P.C.Canfield, *J. Magn. Magn. Mater.*, **205** (1999) 53.
- [3] P.C.Canfield, S.L.Bud'ko, B.K.Cho, A.Lacerda, D.Farrell, E.Johnston-Halperin, V.A.Kalatsky and V.L.Pokrovsky, *Phys. Rev. B*, **55** (1997) 970.
- [4] B.K.Cho, P.C.Canfield, L.L.Miller and D.C.Johnston, *Phys. Rev. B*, **52** (1995) 3684.
- [5] B.K.Cho, P.C.Canfield and D.C.Johnston, *Phys. Rev. B*, **53** (1996) 8499.
- [6] P.C.Canfield, P.L.Gammel and D.J.Bishop, *Phys. Today*, **51**(10) (1998), 40.
- [7] K.D.Myers, P.C.Canfield, V.A.Kalatsky and V.L.Pokrovsky, *Phys. Rev. B*, **59** (1999) 1121.
- [8] V.A.Kalatsky and V.L.Pokrovsky, *Phys. Rev. B*, **57** (1998) 5485.
- [9] A.Yatskar, N.K.Budraa, W.P.Beyermann, P.C.Canfield and S.L. Bud'ko, *Phys. Rev. B*, **54** (1996) R3772.
- [10] G.Knopp, A.Loidl, R.Caspary, U.Gottwick, C.D.Bredl, H.Spille, F.Steglich and A.P.Murani, *J. Magn. Magn. Mater.*, **74** (1988) 341.
- [11] G.Zanicchi, D.Mazzone, V.Contardi, R.Marazza, G.Rambaldi and D.Rossi, *Gazz. Chim. Ital.*, **113** (1983) 257.
- [12] G.Gibson, R.Pttgen, R.K.Kremr, A.Simon and K.R.A.Ziebeck, *J. Alloys Comp.*, **239** (1996) 34.
- [13] S.Baran, M.Hofmann, J.Leciejewicz, B.Penc, M.Slaski and A.Szytula, *J. Alloys Comp.*, 281 (1998) 92.
- [14] Z.Fisk and J.P.Remeika, *Handbook of the Physics and Chemistry of Rare Earths*, Vol.12 (1989), 53.
- [15] P.C.Canfield and Z.Fisk, *Phil.Mag.*, **B65** (1992) 1117.
- [16] P.C.Canfield and I.R.Fisher, *J. Cryst. Growth* **225** (2001), 155.
- [17] R.D.Shannon, *Acta Cryst.* **A32** (1976), 751.
- [18] M.E.Fisher, *Phil. Mag.*, **7** (1962) 1731.
- [19] M.E.Fisher, and J.S.Langer, *Phys. Rev. Lett.*, **20** (1968) 665.
- [20] Y.L.Wang, *Phys. Lett. A*, **35** (1971), 383.
- [21] P.Boutron, *Phys. Rev. B*, **7** (1973), 3226.

- [22] E.Q.T.Morosan, S.L.Bud'ko and P.C.Canfield (unpublished).
- [23] M.D. Daybell, *Magnetism*, edited by H. Suhl (Academic, NY, 1973) v.5, p.129.
- [24] A.C. Hewson, *The Kondo Problem to Heavy Fermions* (Cambridge University Press, Cambridge, 1997).
- [25] A.Yatskar, N.K.Budraa, W.P.Beyermann, P.C.Canfield and S.L.Bud'ko, Phys. Rev. B, **54** (1996), R3772.
- [26] O.Trovarelli, C.Geibel, S.Mederle, C.Langhammer, F.M.Grosche, P.Gegenwart, M.Lang, G. Sparn and F.Steglich, Phys. Rev. Lett., **85** (2000), 626.
- [27] W.P.Beyermann, P.C.Canfield, S.L.Bud'ko, A.Lacerda, Bull. Am. Phys. Soc. **43**(1) (1998), C31-8, 115.
- [28] K.Katoh, Y.Mano, K.Nakano ,G.Terui, Y.Niide and A.Ochiai, J. Magn. Magn. Mater., in press.
- [29] D.R.Noakes and G.K.Shenoy, Phys.Lett. **91A** (1982), 35.
- [30] E.V. Sampathkumaran, K. Sengupta, S. Rayaprol, K.K. Iyer, Th. Doert, and J.P.F. Jemetio, Phys. Rev. Lett., **91** (2003), 36603.
- [31] J.D.Thompson and J.M.Lawrence, *Handbook on the Physics and Chemistry of Rare Earths*, edited by K.A.Gschneidner et al., v.19 (Elsevier, Amsterdam, 1994) p.383.

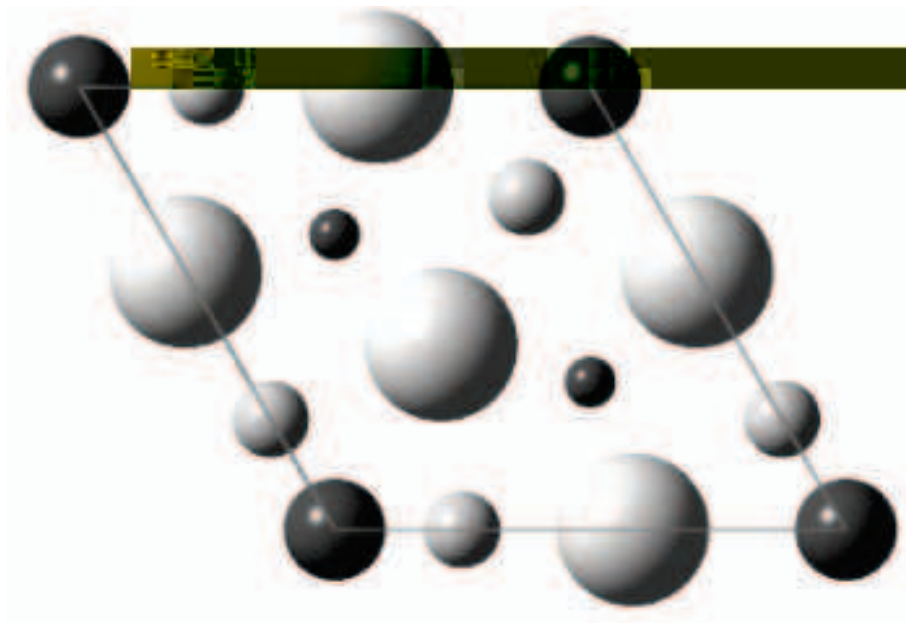


Fig. 1. *c*-axis projection of the RAgGe crystal structure. R - light large circles and Ge - dark medium circles form  $R_3Ge$  layers; Ag - smaller light and Ge - small dark circles form  $Ag_3Ge_2$  layer.

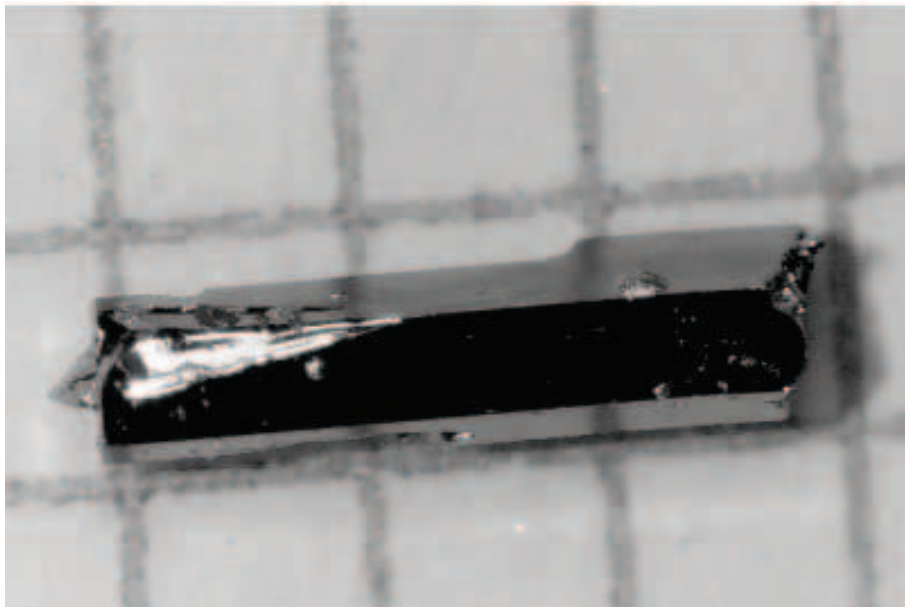


Fig. 2. Single crystal of YbAgGe, with approximate dimensions  $0.4 \times 0.4 \times 3.0$  mm. Hexagonal rod geometry evident (three of the six possible facets are visible here); a few AgGe flux droplets can be seen on the surface of the crystal.



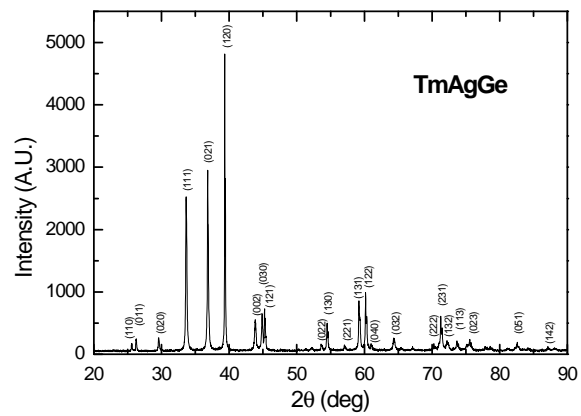


Fig. 3. Powder X-ray diffraction pattern for TmAgGe. Peaks are indexed to a hexagonal structure, with  $a = 7.0565\text{\AA}$  and  $c = 4.1454\text{\AA}$ .

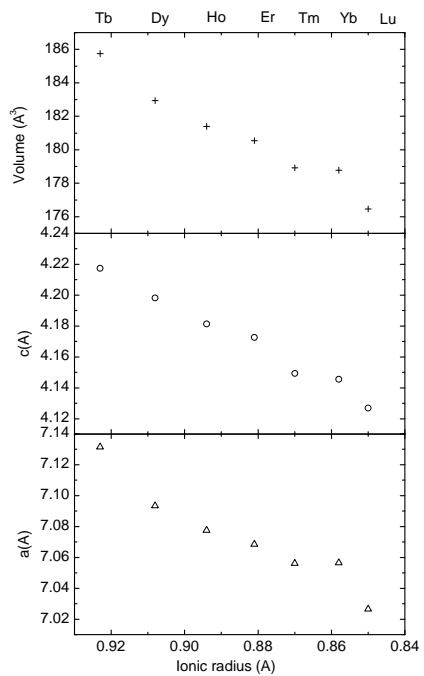


Fig. 4. Unit cell volumes and lattice parameters for RAgGe, R=Tb-Lu as a function of  $R^{3+}$  ionic radius (bottom axis) or rare earth (upper axis).

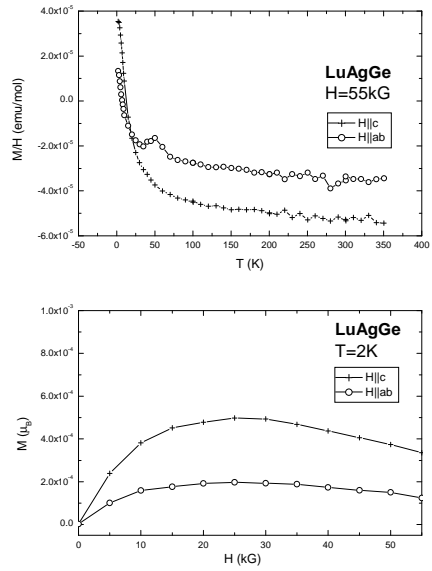


Fig. 5. (a) Anisotropic temperature-dependent susceptibility and (b) anisotropic magnetization isotherms at  $T=2\text{K}$  of LuAgGe.

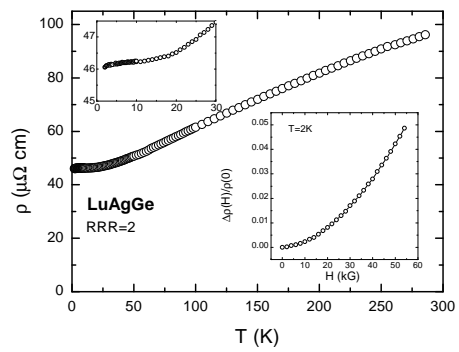


Fig. 6. Zero-field resistivity (upper left insert - low temperature part) and transverse magnetoresistance (lower right insert) of LuAgGe.

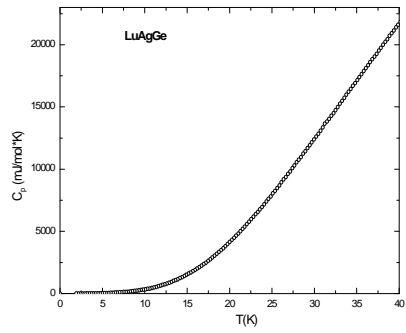


Fig. 7. Heat capacity of LuAgGe.

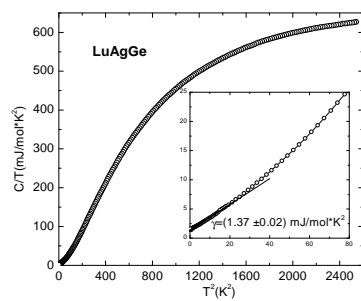


Fig. 8.  $C_p/T$  versus  $T^2$  for LuAgGe; insert: low temperature part, line in the inset is a linear fit at low temperatures.

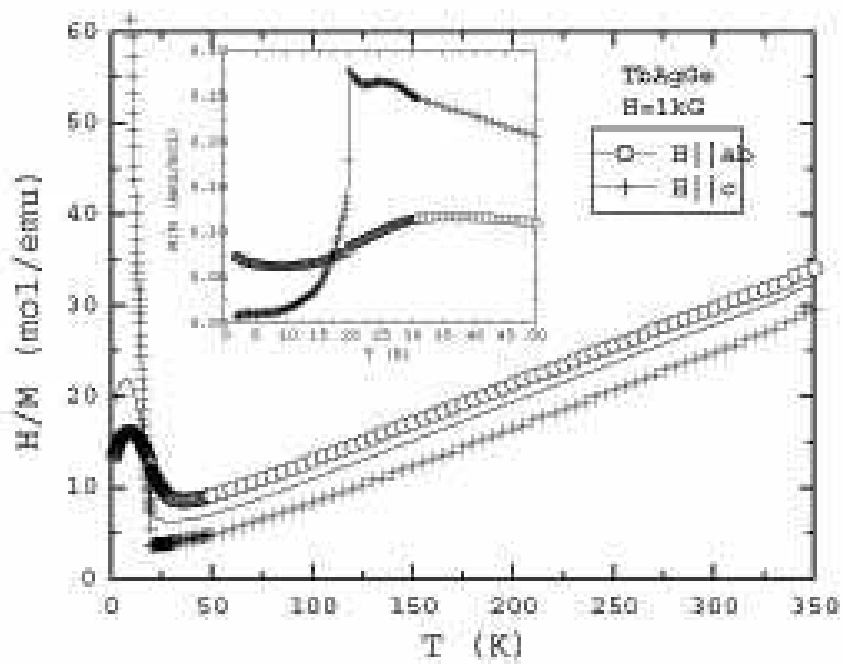


Fig. 9. Anisotropic inverse susceptibilities of TbAgGe and calculated average (line); inset: low-temperature anisotropic susceptibilities.

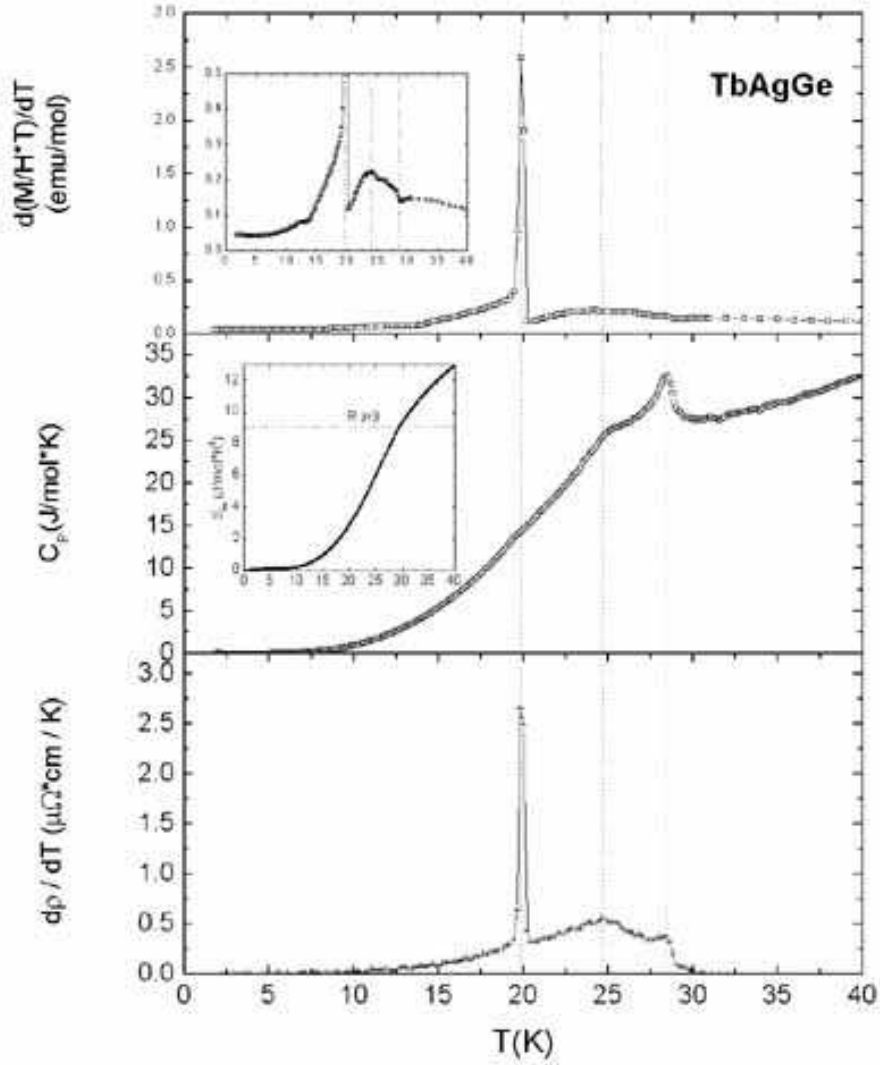


Fig. 10. (a) Low-temperature  $d(\chi T)/dT$  for TbAgGe (inset: enlarged to show lower peaks' position in  $d(\chi T)/dT$ ); (b) specific heat  $C_p(T)$  with the magnetic entropy  $S_m$  in the inset; (c) low-temperature  $d\rho/dT$ ; dotted lines mark the peak positions as determined from (a).



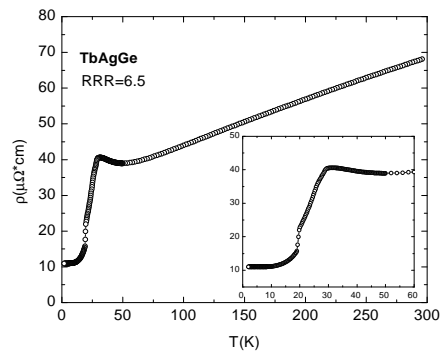


Fig. 11. Zero-filed resistivity of TbAgGe (inset: enlarged low-temperature part).

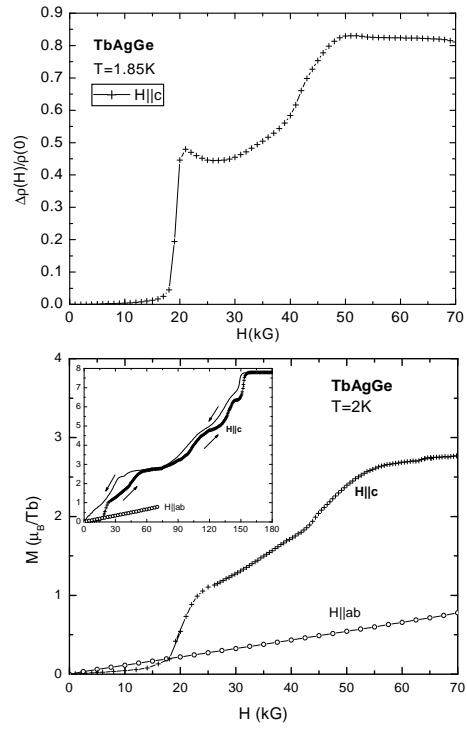


Fig. 12. (a) Transverse magnetoresistance for TbAgGe; (b) anisotropic magnetization curves for  $H$  up to 70kG (inset:  $M(H, T=2\text{K})$  for increasing and decreasing field  $H\parallel c$ , up to  $H=180\text{kG}$ ).

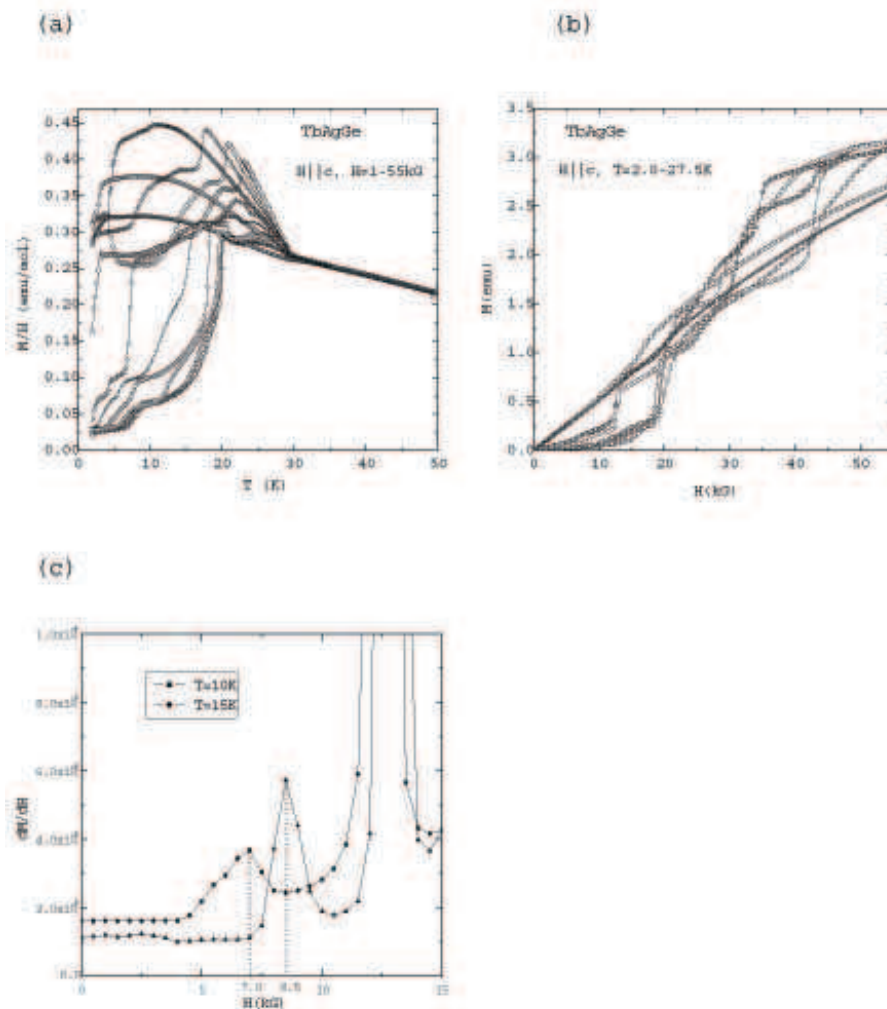


Fig. 13.  $\chi(T)$  curves for various (1, 2.5, 5, 7.5, 10, 12.5, 15, 20, 25, 30, 35, 45, 55 kG) fields (a) and several  $M(H)$  ( $T = 2, 3, 4, 6, 10, 20, 25, 27, 50$  K) isotherms (b); (c) - enlarged derivatives of  $M(H)$  (for  $T=10$ K and  $15$ K) as an example of how the lower line in the phase diagram was obtained.

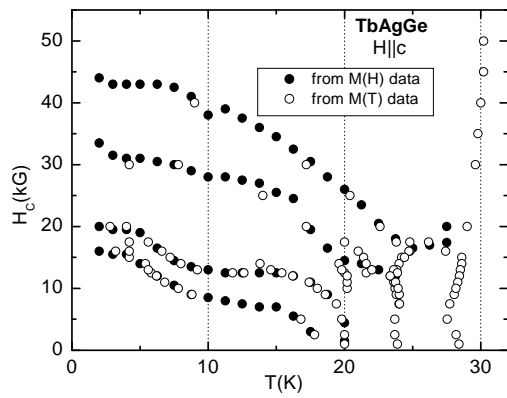


Fig. 14.  $H_c - T$  phase diagram as determined from the magnetization curves in Fig. 13.

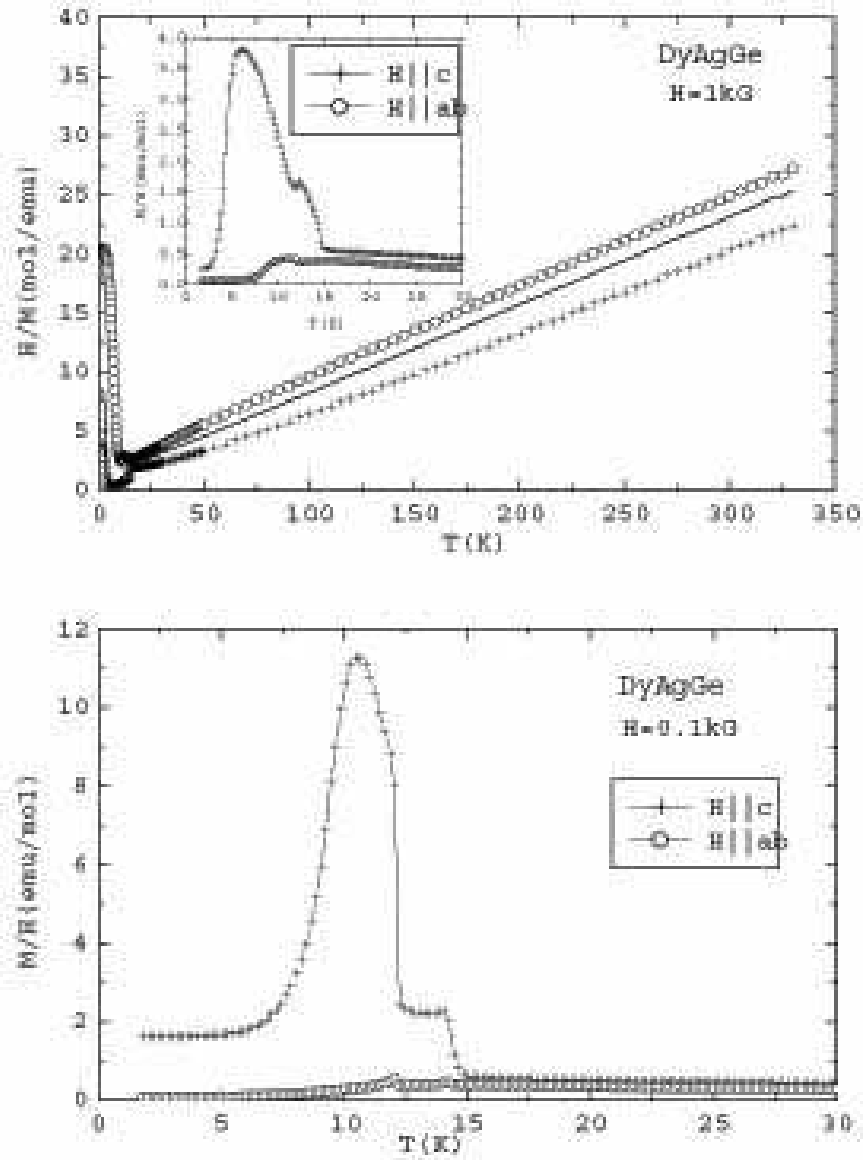


Fig. 15. (a) Anisotropic inverse susceptibilities of DyAgGe and calculated average (line) at  $H=1\text{kG}$ ; inset: low-temperature anisotropic susceptibilities; (b) low-temperature anisotropic susceptibilities for  $H=0.1\text{kG}$ .

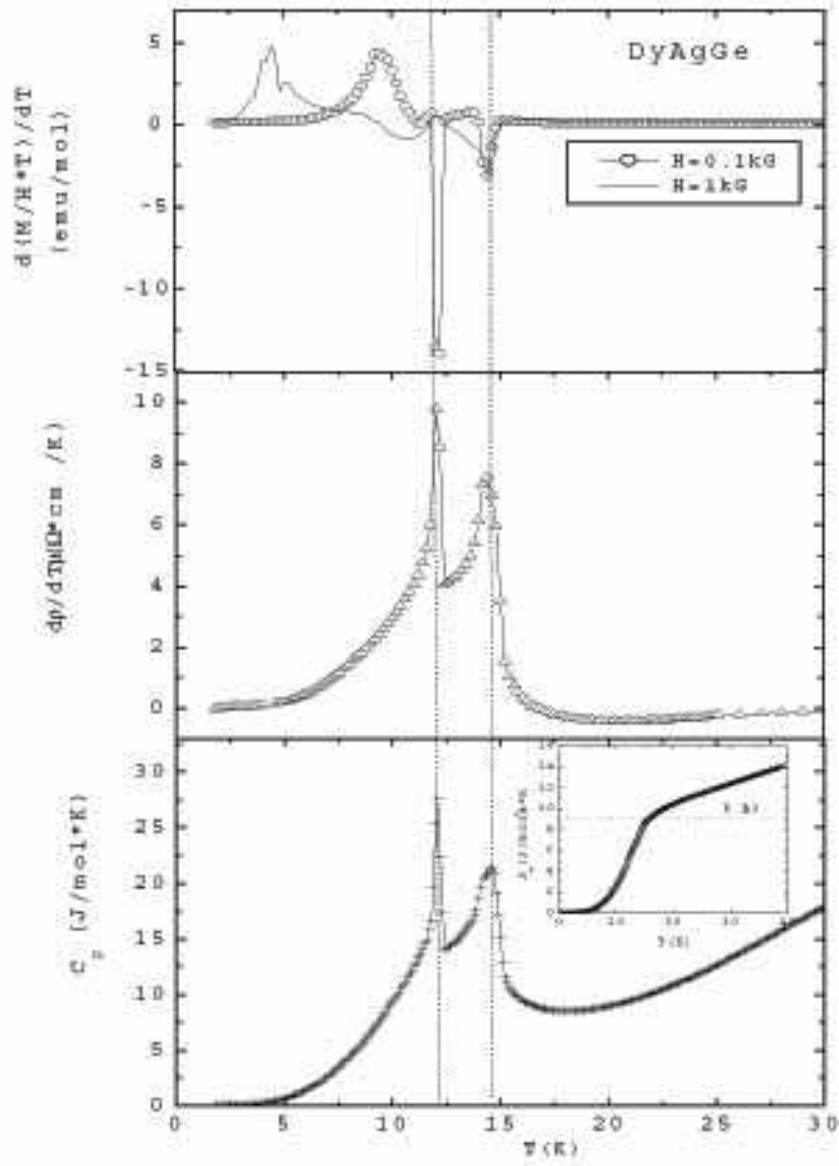


Fig. 16. (a) Low-temperature  $d(\chi T)/dT$  for TbAgGe for  $H=0.1$  kG and 1 kG; (b) low-temperature  $d\rho/dT$ ; (c) specific heat  $C_p(T)$  with the magnetic entropy  $S_m$  in the inset; dotted lines mark the peak positions as determined from lowest field data in (a).

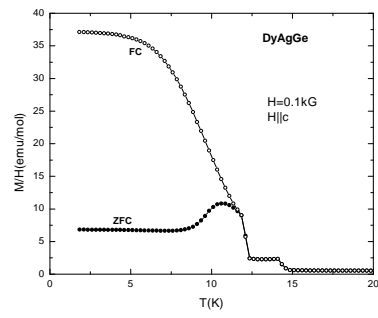


Fig. 17. ZFC-FC magnetization of DyAgGe,  $H=0.1\text{kG}$  ( $H\parallel c$ ).

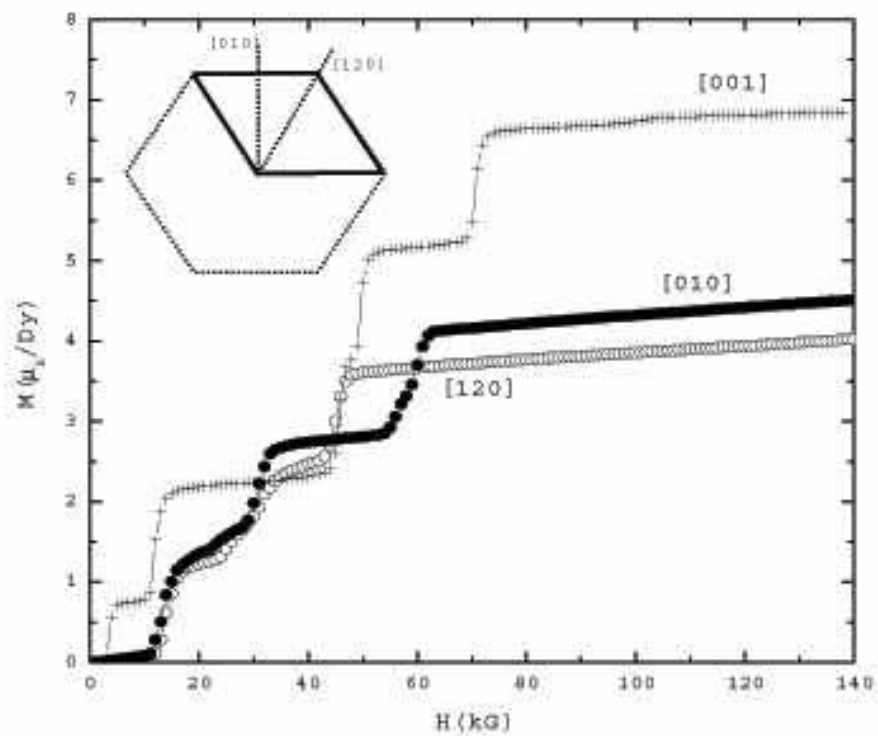


Fig. 18. Anisotropic magnetization curves shown for three orientations of the applied field.



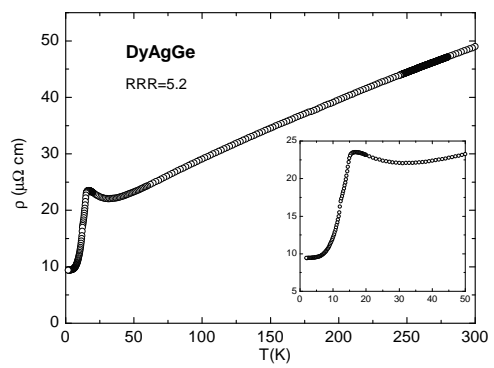


Fig. 19. Zero-field resistivity of DyAgGe (inset: enlarged low-temperature part).

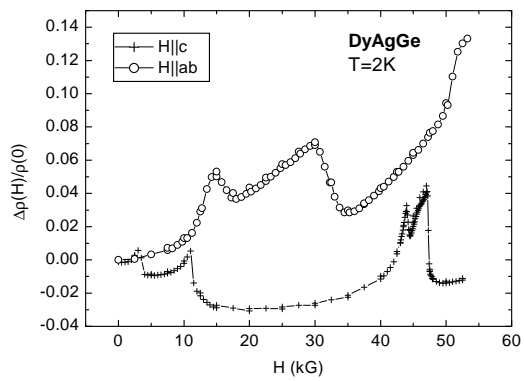


Fig. 20. Anisotropic magnetoresistance at T=2K.

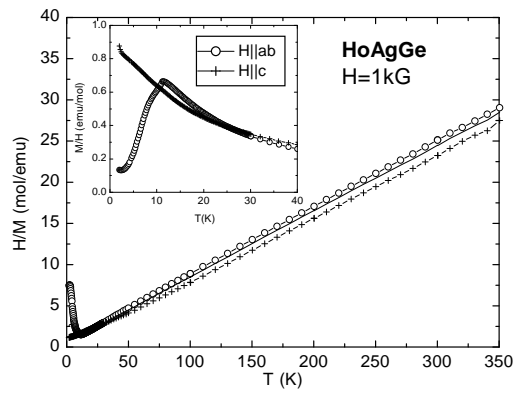


Fig. 21. Anisotropic inverse susceptibilities of HoAgGe and calculated average (line); inset: low-temperature anisotropic susceptibilities.

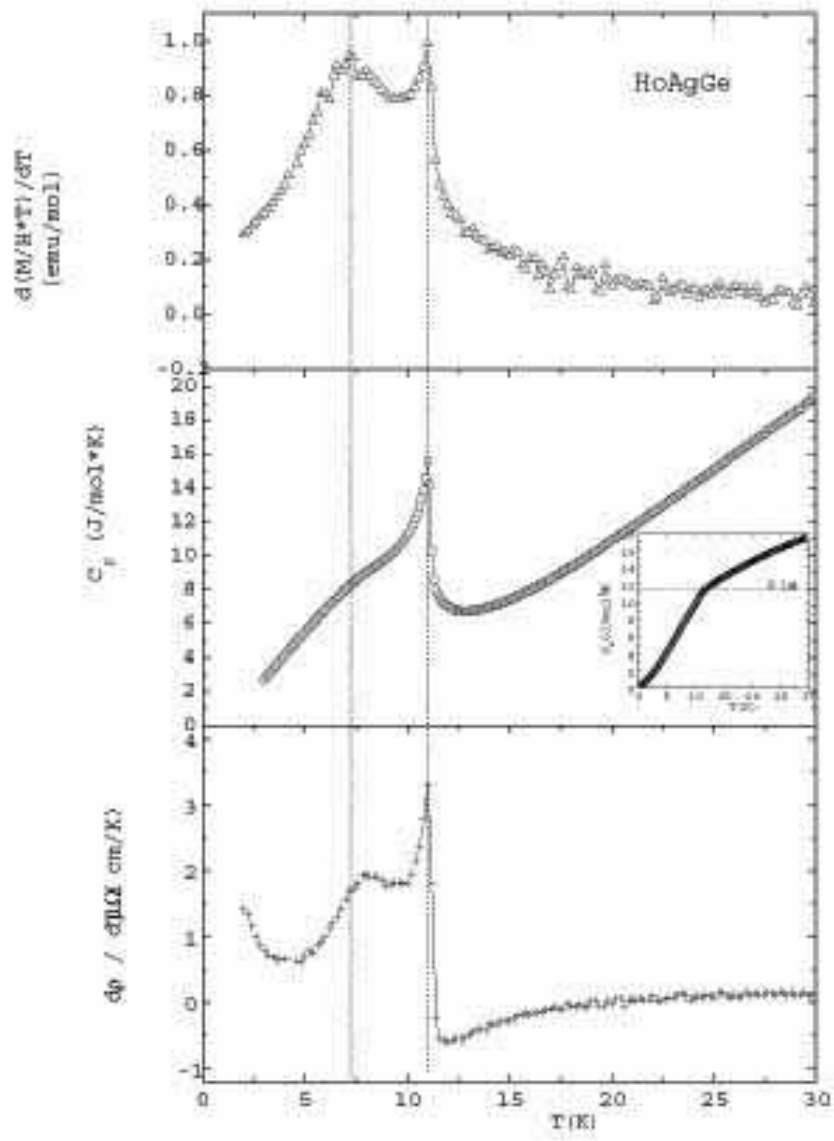


Fig. 22. (a) Low-temperature  $d(\chi T)/dT$  of HoAgGe; (b) Specific heat  $C_p(T)$  with the magnetic entropy  $S_m$  in the inset; (c) low-temperature  $d\rho/dT$ ; dotted lines mark the peak positions as determined from (a).

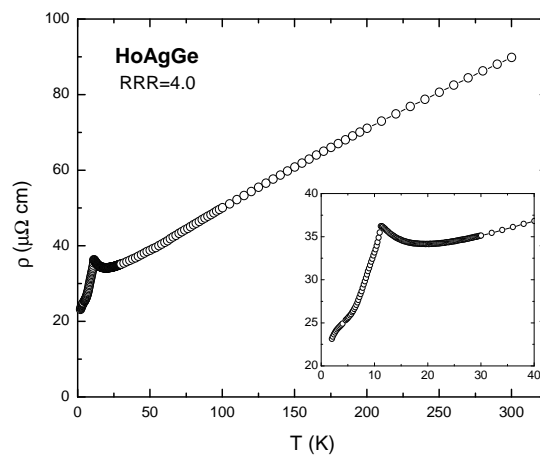


Fig. 23. Zero-field resistivity of HoAgGe (inset: enlarged low-temperature part).

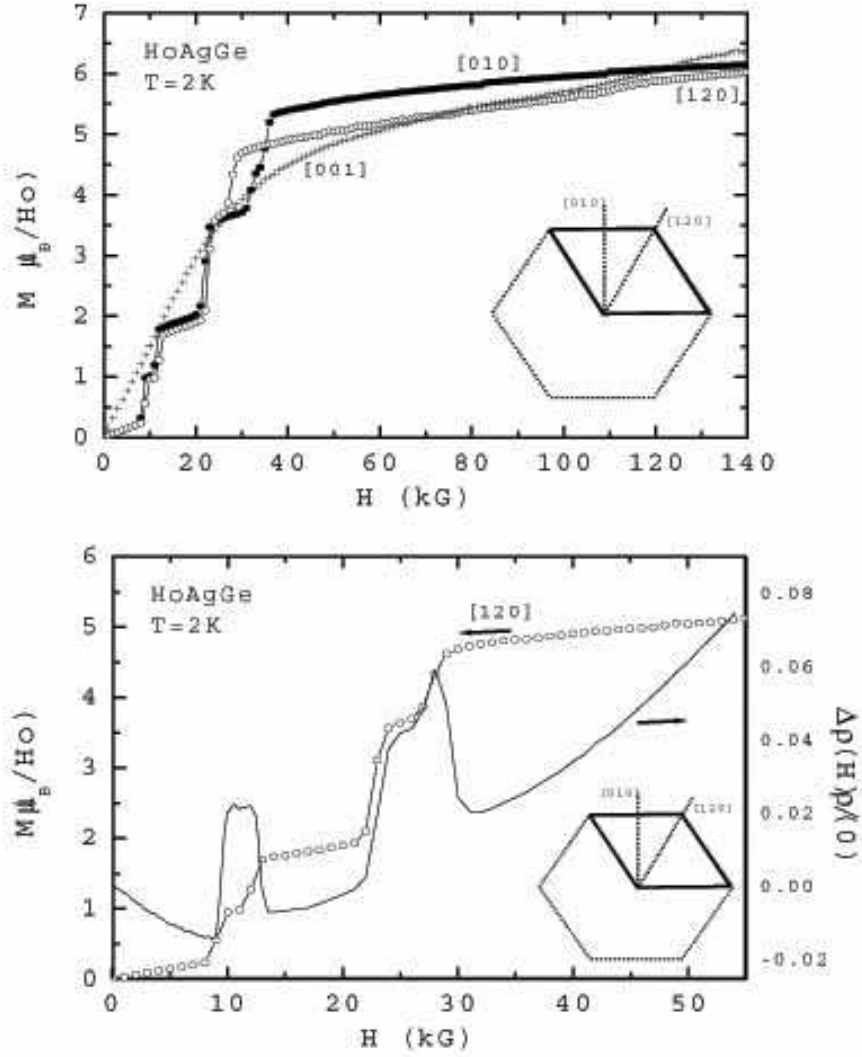


Fig. 24. (a) Anisotropic magnetization curves in HoAgGe, shown for three orientations of the applied field at  $T=2\text{K}$ ; (b) Transverse magnetoresistance and  $M(H)$  for  $H\parallel[120]$  at  $T=2\text{K}$ .

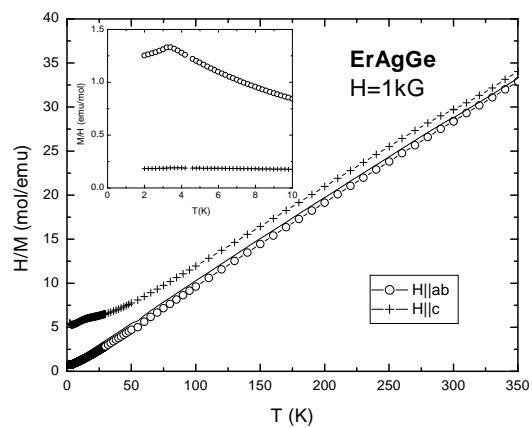


Fig. 25. Anisotropic inverse susceptibilities of ErAgGe and calculated average (line); inset: low-temperature anisotropic susceptibilities.

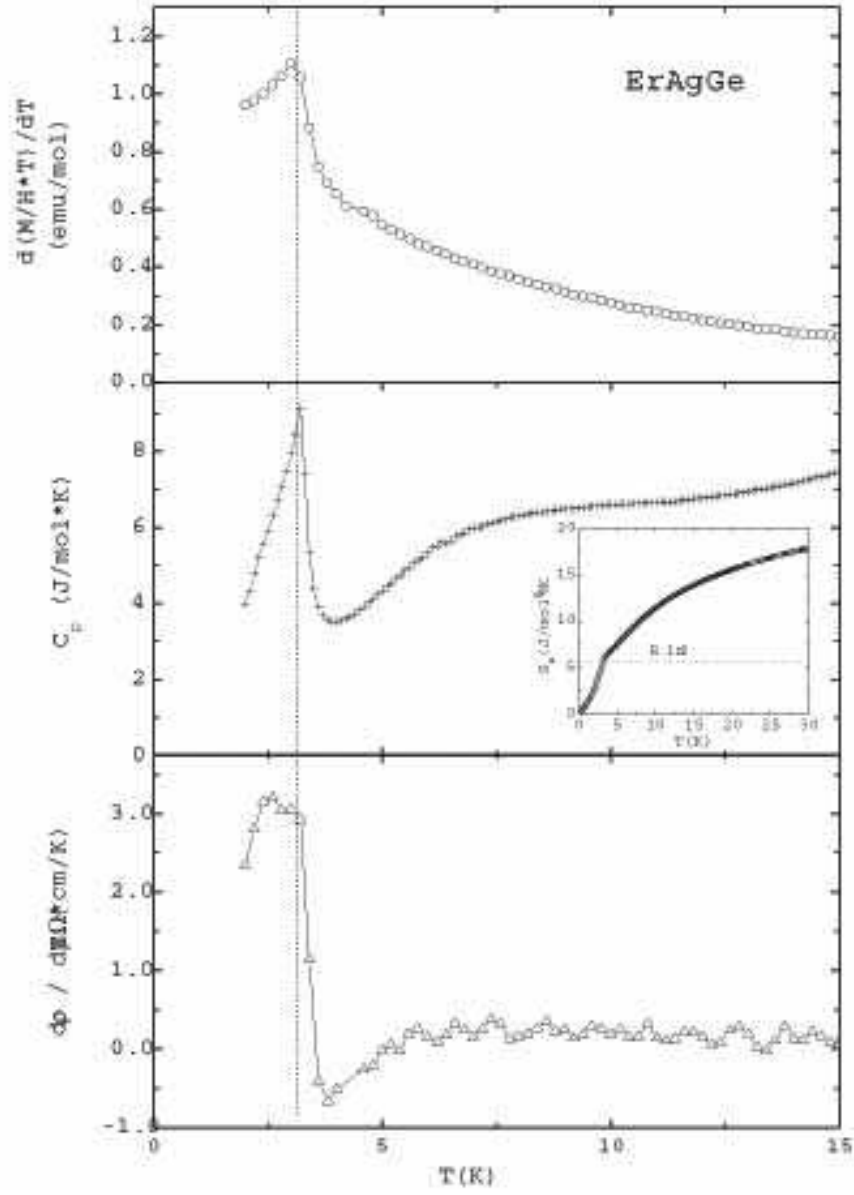


Fig. 26. (a) low-temperature  $d(\chi T)/dT$  of ErAgGe ; (b) Specific heat  $C_p(T)$  with the magnetic entropy  $S_m$  in the inset; (c) low-temperature  $d\rho/dT$ ; dotted line mark the peak position as determined from (b).



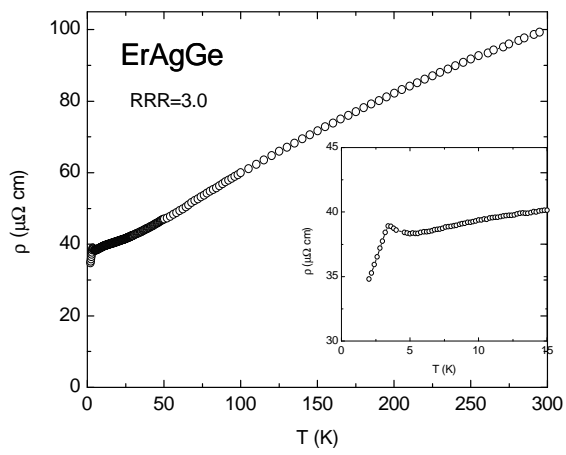


Fig. 27. Zero-field resistivity of ErAgGe (inset: enlarged low-temperature part).

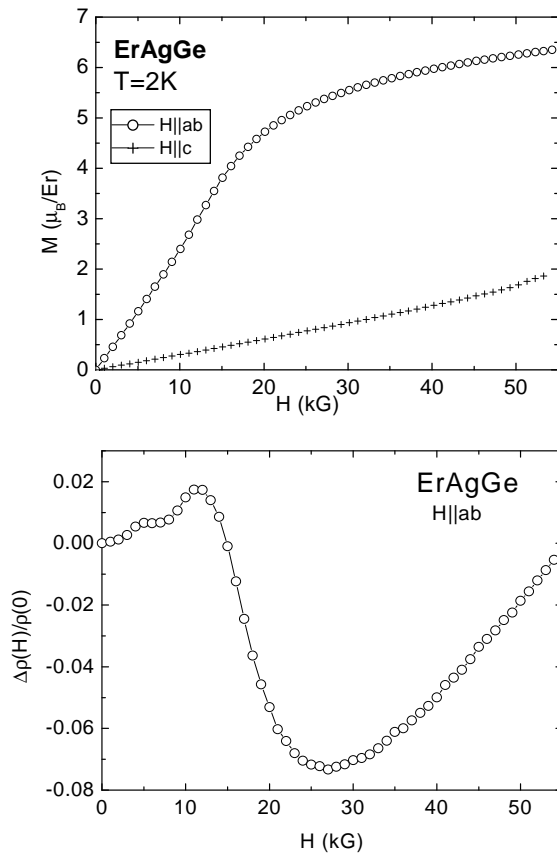


Fig. 28. (a) Anisotropic field-dependent magnetization for ErAgGe at  $T=2\text{K}$ ; (b) transverse magnetoresistance at  $T=2\text{K}$ .

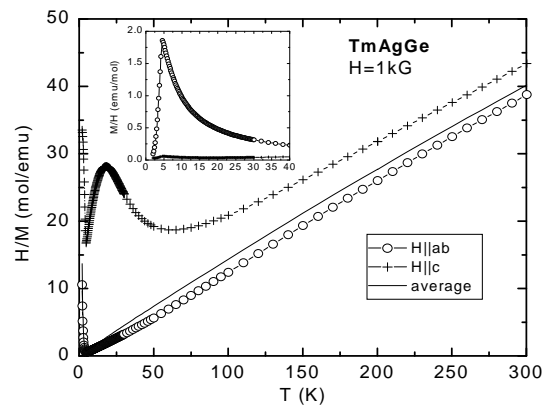


Fig. 29. Anisotropic inverse susceptibilities of TmAgGe and calculated average (line); inset: low-temperature anisotropic susceptibilities.

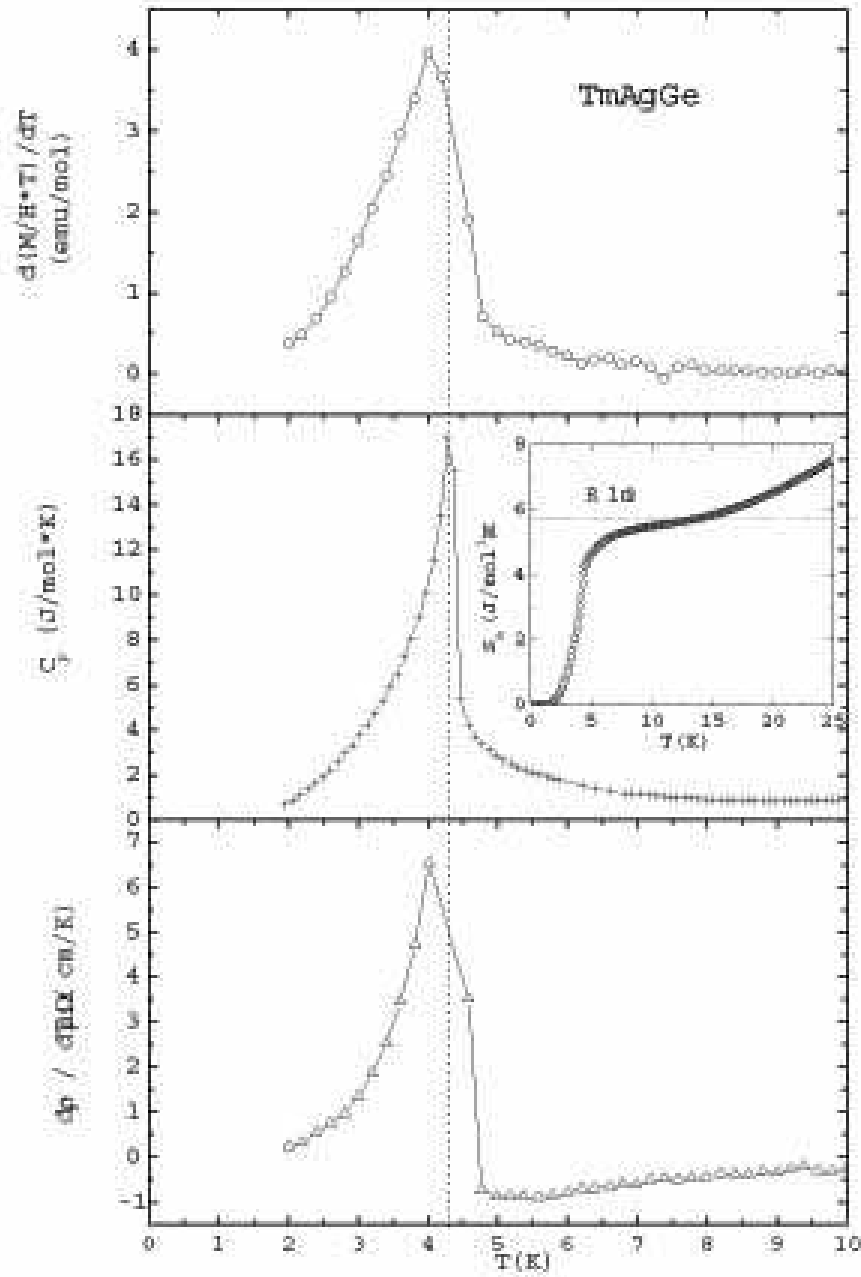


Fig. 30. (a) Low-temperature  $d(M/H * T)/dT$  for TmAgGe; (b) specific heat  $C_p(T)$  with the magnetic entropy  $S_m$  in the inset; (c) low-temperature  $d\rho/dT$ ; dotted line marks the peak position as determined from (a).

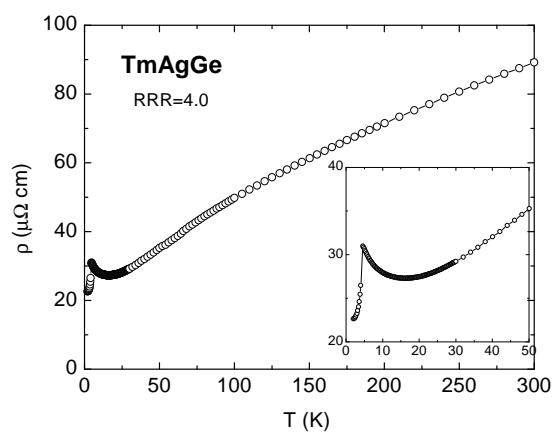


Fig. 31. Zero-field resistivity of TmAgGe (inset: enlarged low-temperature part).

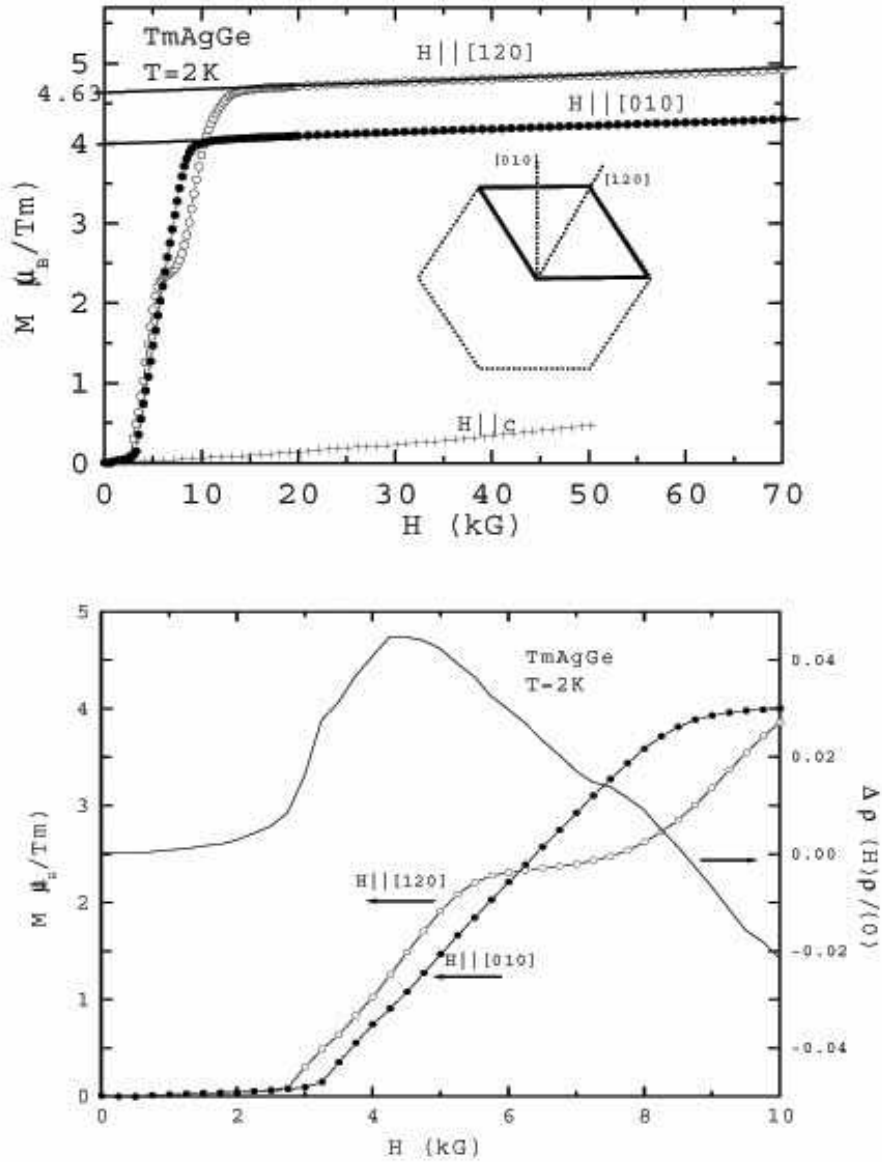


Fig. 32. (a) Anisotropic magnetization curves in TmAgGe, shown for three orientations of the applied field; (b) Transverse magnetoresistance and  $M(H)$  curves for  $H||ab$ , at  $T=2\text{K}$ .

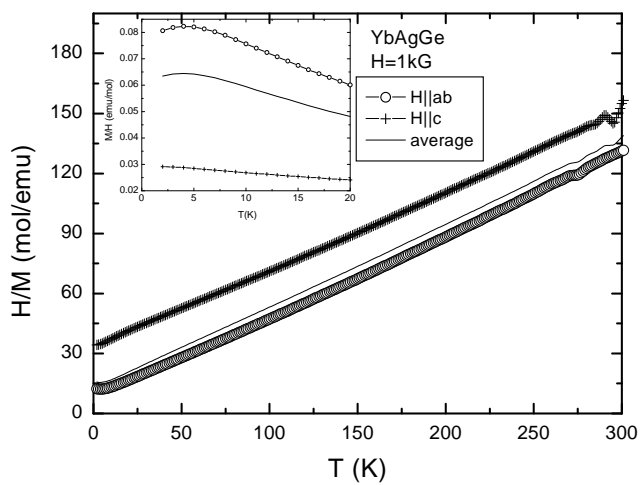


Fig. 33. Anisotropic inverse susceptibilities of YbAgGe and calculated average (line); inset: low-temperature anisotropic susceptibilities.

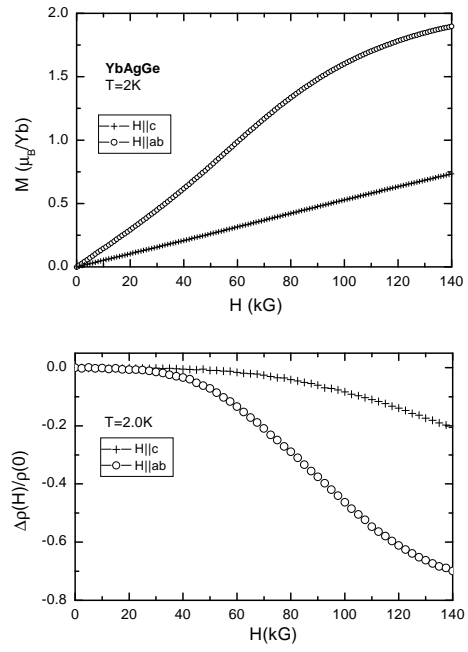


Fig. 34. (a) Anisotropic field-dependent magnetization and (b) magnetoresistance for YbAgGe at  $T=2\text{K}$ .



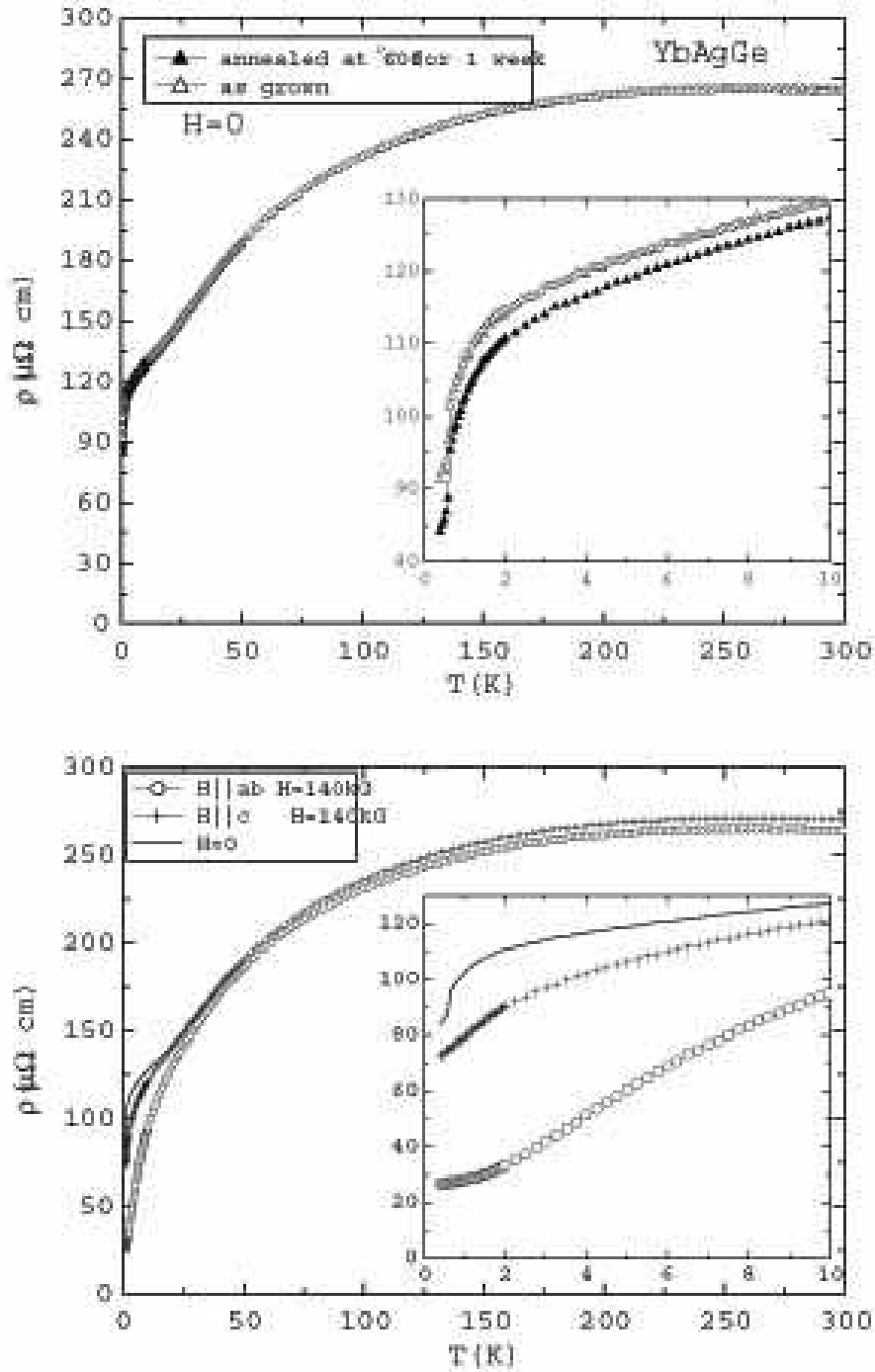


Fig. 35. (a) Zero-field resistivity of as grown and annealed YbAgGe, (inset: enlarged low-temperature part); (b) anisotropic transverse resistivity for annealed YbAgGe in applied field  $H=140\text{kG}$  (small symbols) and for  $H=0$  (line).

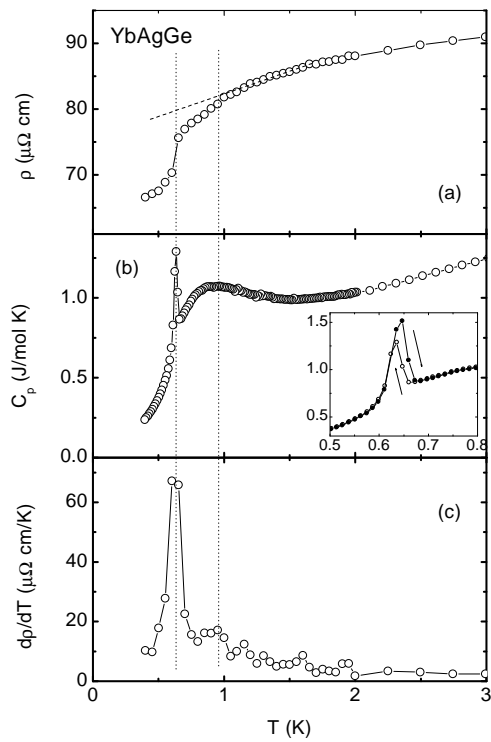


Fig. 36. Low temperature part of (a) resistivity; (b) specific heat (inset:  $C_p(T)$  on warming and cooling); (c)  $d\rho/dT$ . Lines mark magnetic transitions.

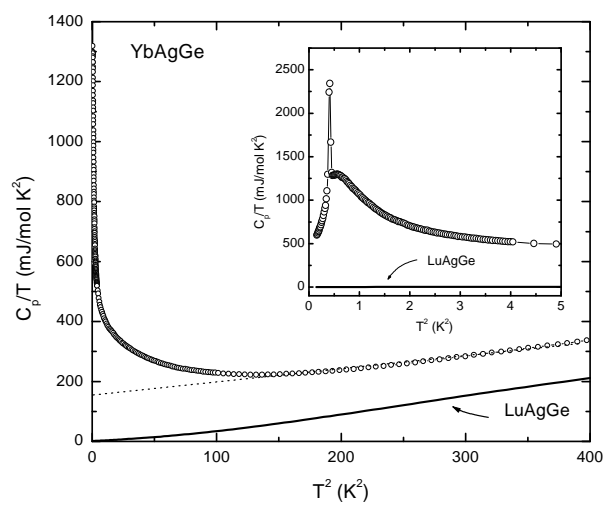


Fig. 37.  $C_p(T^2)/T$  for YbAgGe (open circles) with a high temperatures linear fit (dotted line) giving  $\gamma$  value of  $(154.2 \pm 2.5)$   $\text{mJ/mol K}^2$ ; line:  $C_p(T^2)/T$  for non-magnetic LuAgGe. Inset: low temperature part.

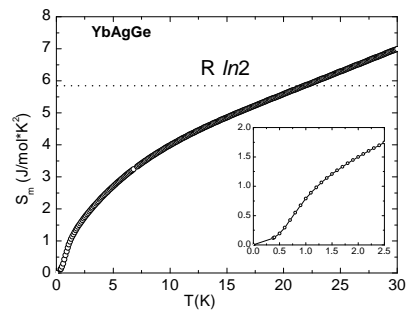


Fig. 38. Magnetic entropy for  $\text{YbAgGe}$ . Inset: low temperature part.

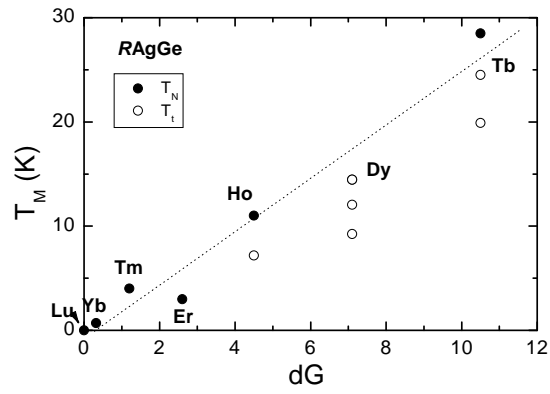


Fig. 39. Changes of the magnetic ordering temperatures  $T_m$  for  $R=\text{Tb-Lu}$  in the  $R\text{AgGe}$  series, with the de Gennes scaling parameter  $dG$  (the dotted line represents the expected linear dependence).

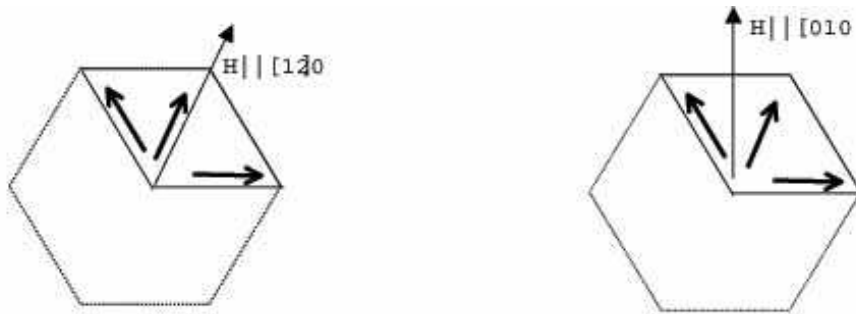


Fig. 40. Hexagonal unit cell with the magnetic moments (short arrows) in the saturated state of TmAgGe; long arrows indicate the field along the two high-symmetry directions of the crystal.

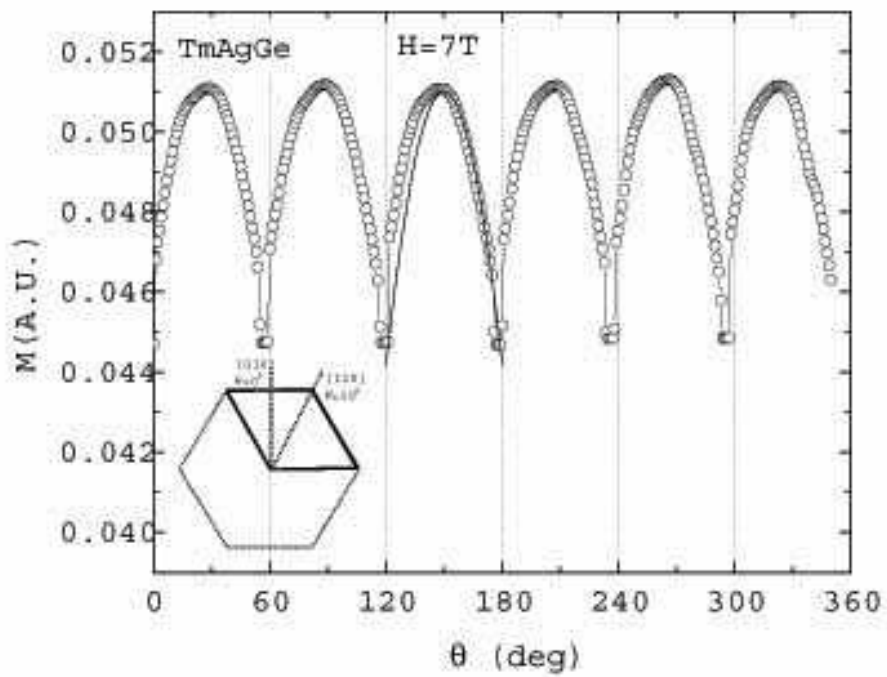


Fig. 41. Angular dependent magnetization in TmAgGe, for  $H=70\text{kG}$  applied in the  $ab$ -plane (the solid line shown for  $\theta = 120 - 180^\circ$  is  $M(\theta) \sim \cos(\theta - 30^\circ)$ , as expected from model).